LSU Master's Theses   Graduate School

2007

Impingement Heat Transfer In The Leading Edge Cavity Of A Gas Turbine Vane

Amar Jeetendra Panchangam Nivarthi
Louisiana State University and Agricultural and Mechanical College

IMPINGEMENT HEAT TRANSFER IN THE LEADING EDGE CAVITY OF A GAS TURBINE VANE

Submitted to the Graduate Faculty of the
Louisiana State University and
Agricultural and Mechanical College
in partial fulfillment of the
requirements for the degree of
Master of Science in Mechanical Engineering

in

The Department of Mechanical Engineering

by
Amar Jeetendra Panchangam Nivarthi
B.S., Osmania University, Hyderabad, India, 2004
May 2008

Acknowledgements

Table of Contents

Abstract

Jet Impingement Cooling is an internal cooling technique used in the leading edge cavities of Turbine Vanes. This involves a series of jets impinging onto the internal surfaces of a turbine vane/blade through the impingement plate. For the model tested here, the area around the blade/vane leading edge was studied for both heat transfer performance and aerodynamics losses. The performance of an Impingement cooling system depends on parameters like the spent flow effect on the downstream jet, film cooling configuration, and tip flow condition. The present study focuses on analyzing the effect of these parameters on a unique impingement cooling configuration. A Liquid Crystal based technique was used to obtain the heat transfer distribution on the target surface. A novel Camera-Endoscope combination was used to capture the liquid crystal images in a confined space. Heat Transfer Contours were obtained for a total of six different cases based on differing film cooling hole configurations and tip condition. Peak heat transfer values are observed in the impingement zone along with a characteristic reduction in heat transfer as we move away from the impingement zone. The results indicated that the cross flow had a negative impact on the peak heat transfer value but improved the uniformity of heat transfer distribution. The film cooling configuration was found to affect the amount of cross flow and the location of the impingement zone of the jet. The cross flow effect is found to have reduced effect with an increase in the available number of film cooling holes leading to an increase in the peak heat transfer. The tip condition was altered for the last case in which it adversely affected the extent of jet impingement. Line plots for all the contours showed the spent flow effect. A fluid dynamic analysis of all the above effects was presented.

Chapter 1

Introduction

The gas turbine is extensively used as a power plant for aircraft propulsion and power generation. The main components of a gas turbine are the compressor, combustion chamber and the turbine. A schematic of all the stages is shown in Fig 1.1*(i)*. The schematic can be represented by a closed thermodynamic cycle shown in Fig 1.1*(ii)*. The cycle has four stages, representing the physical phenomena taking place at different sections of a gas turbine at the same time. The fresh air enters the compressor (1-2) where it undergoes a compression. The typical compressor efficiency is around 85% to 88% for a modern design. However, for simplicity, an isentropic compression was used here. Subsequently the compressed air flows into the combustion chamber where it mixes with the fuel and is ignited resulting in energy addition (2-3) to the flow. In this process, the small pressure loss is mainly due to flow mixing and the viscous effect, thus a constant pressure process was used here. The hot gas mixture of air and combustion products then enters the turbine where it expands to the low back pressure (3-4) and produces power. The irreversibility loss in the expansion is small thus an isentropic process can be used in the first approximation. A part of this power is used to drive the compressor and the rest is extracted from the system as either thrust (jet engine) or shaft work (power production). As with any internal combustion engine the main aim is to achieve better performance and reliability. The demand for fuel efficient and higher thrust engines has posed a huge challenge to the engineers. Both thermal efficiency and thrust output increase with increasing Turbine Inlet Temperature. This dependence illustrated in the Fig 1.2 below.

(i)   *(ii)*
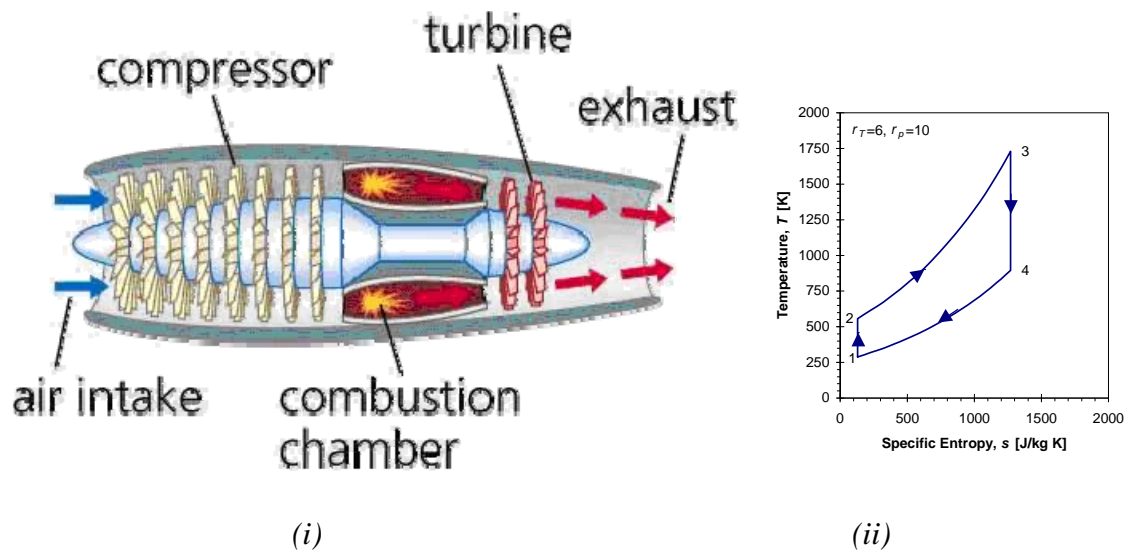
Fig 1.1: Gas Turbine Schematic and thermodynamic cycle [1]
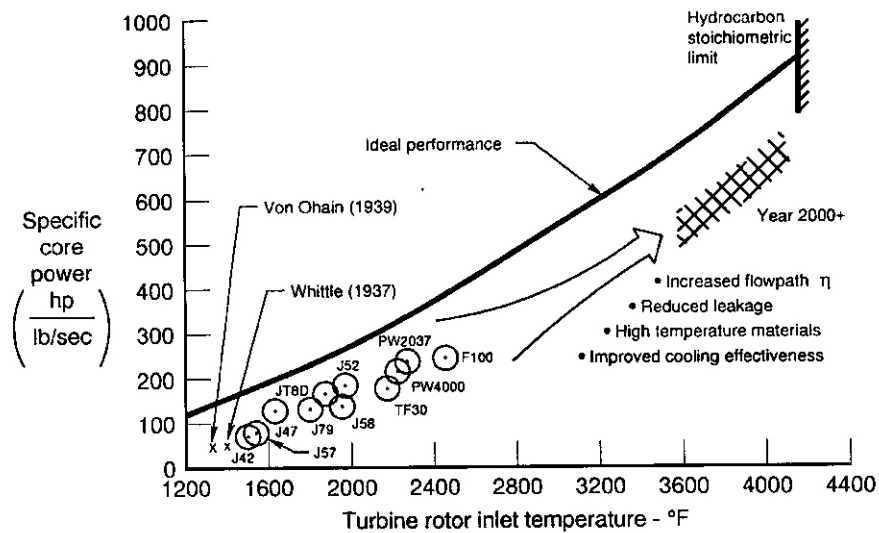
Fig 1.2: Increase in Specific Core Power with Increasing Inlet Temperature
(Saunter et al., 1992)

The limiting factor to increasing turbine inlet temperature is the permissible

operating temperature of the blade material. Therefore cooling of the blades is the only

way to use the existing blade material with increased inlet temperatures. The modern gas

2

turbine blades have both internal as well surface cooling mechanisms which utilize the air extracted from the compressor. Cooling is crucial to safeguard the engine for normal operation, also the cooling leads to a reduced thermal efficiency, an optimized cooling technique has to be developed.

Figure 1.3 shows the schematic of a blade cooling system that is both internally and externally cooled. As mentioned above, the compressor provides the coolant air to the cooling passages. The coolant passes from the trailing edge, where a pin fin system is used to maximize heat transfer, through the internal cooling passages and rib turbulators into the leading edge. The leading edge region has a plate with a number of holes which provides a jet impingement cooling mechanism on the inner surface of the cavity. The coolant is then ejected through a row of holes on the leading edge itself known as the film cooling holes. The exiting air acts as a protective film between the outer surface of the leading edge and the incoming hot mainstream air.

1.1 Impingement Cooling

Jet impingement heat transfer is one of the most effective heat transfer enhancement techniques in the internal cooling of gas turbine vanes. This involves the impingement of a fluid jet on the internal surface of the leading edge of a vane/blade to provide an extremely high rate of cooling. The heat transfer distribution around a turbine vane is shown in Fig 1.4. Jet impingement heat transfer is suitable for the leading edge of a vane, where the thermal load is highest and a thicker cross-section enables accommodation of a coolant plenum and impingement holes. Jet impingement cooling is capable of providing an extremely high peak heat transfer coefficient for the region under

the impingement jet. The mechanism of heat transfer of a jet impinging a target surface is

illustrated in Fig 1.5
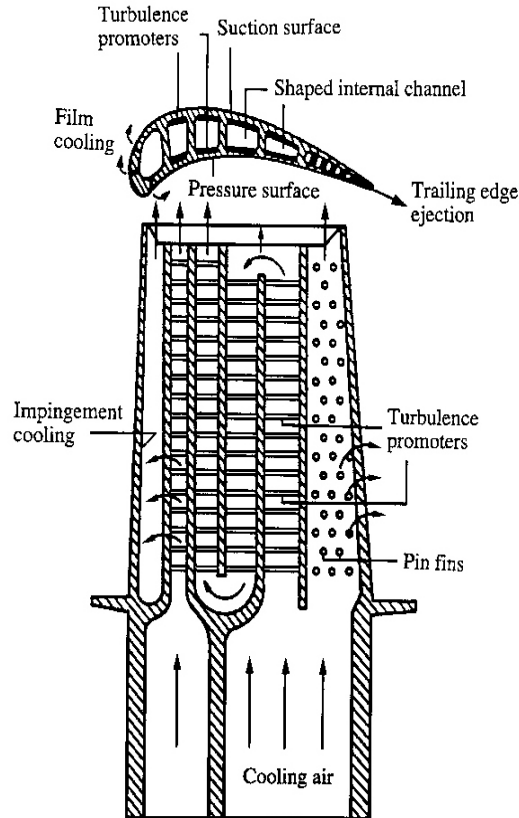
Fig 1.3: Schematic of a cooling system in a Modern Multi-Pass Turbine Blade
(Han, Dutta and Ekkad, 2000)

The jet after impinging spreads along the target surface providing a thin stagnant

boundary layer. A stagnant core is formed at the point where the jet impinges. The

coolant in the stagnant core is continuously replaced by the jet thus providing a step

change in temperature at any given point in time. This creates an extremely high peak in

the heat transfer. As the coolant fluid moves away from the core, heat transfer takes place

in the convection mode at a comparatively lesser rate. A typical heat transfer distribution

in a jet impingement system is shown in Fig 1.6. As evident from Fig 1.6, although the jet

4
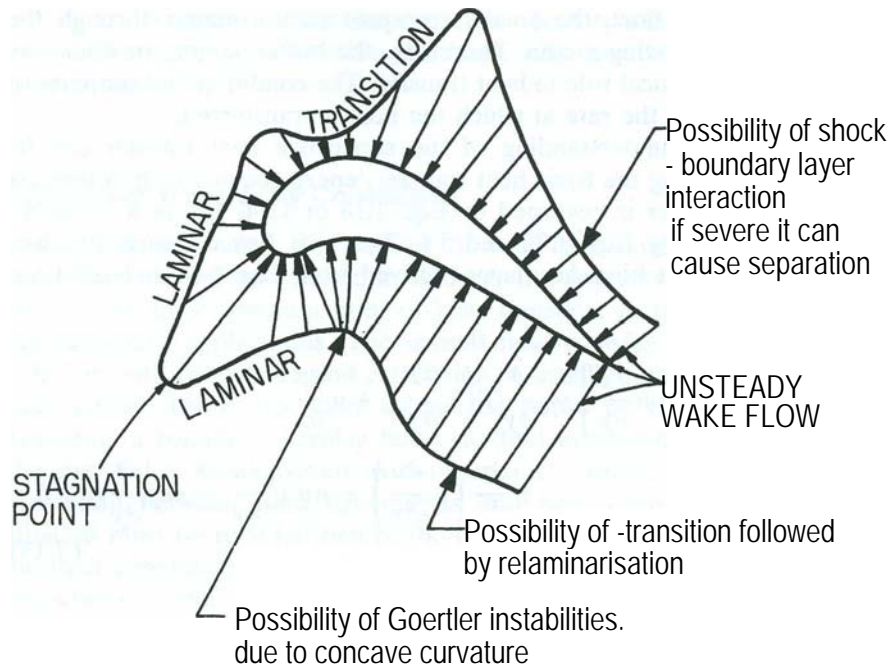
Fig 1.4: Variation of heat transfer rate around a turbine vane
(Han, Dutta and Ekkad, 2000)

impingement cooling has the advantage of achieving significantly enhanced overall heat

transfer rates it inherently suffers from a highly non uniform cooling distribution.

Therefore a number of jets are used in tandem to provide a more uniform heat

transfer distribution. This gives rise to design concerns such as the effect of spent flow

from the upstream jets on the downstream jets and interference between impingement

flows of adjacent jets. Designers have to therefore employ a host of geometric parameters

like the hole geometry, shape & size and spacing of the holes to optimize the heat transfer

distribution. Also other parameters like to jet to cross flow ratio and positioning of the

jets with respect to film cooling holes have to be considered in the design process.

1.2 Literature Survey

Research results during the past four decades on jet impingement heat transfer are

available in a large body of literature. Livingood and Hrycak, 1973, Martin, 1977, Downs

and James, 1987, and Humber and Viskanta, 1994, have provided extensive reviews of
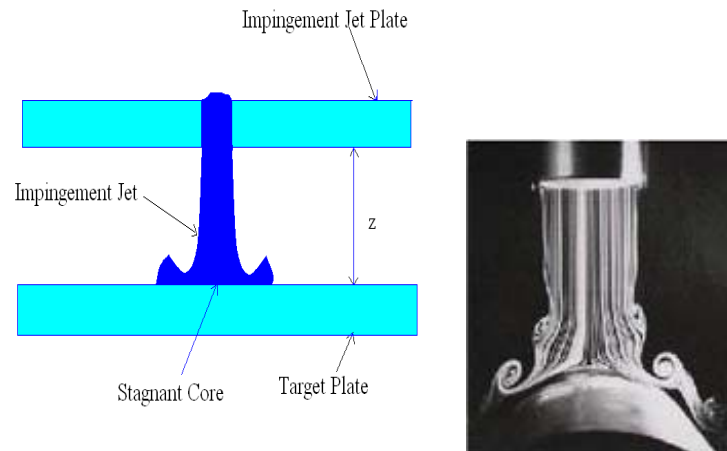
Fig 1.5: Illustration of Jet Impingement and Flow visualization photograph
(http://www.me.umn.edu)
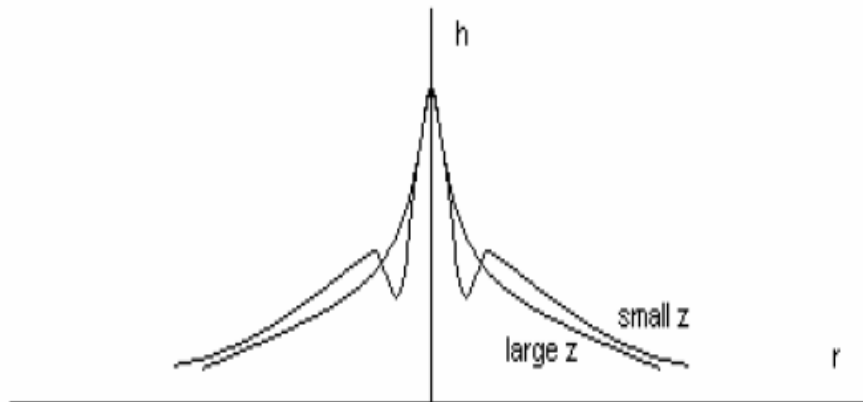
Fig 1.6: Heat Transfer Distribution in a Jet Impingement System
(Bruchez and Goldstein, 1975)

previous literature. Both analytical and numerical studies were performed. Early research

showed that the predominant factor in jet impingement heat transfer is the effect of the

spent flow. Goldstein and Timmers, 1982, showed that spent air from upstream jets

tended to lower local heat transfer coefficients and, in the limit, a flow visualization

showed that the cross flow can sweep away the downstream jets such that the jet impingement was prevented. A series of studies of jet impingements heat transfer under the effect of imposed (external) cross flow in addition to the existing spent flow were conducted. Florschuetz et. al., 1980, 1981, 1984, and Florschuetz, 1982, found that increasing the ratio between the imposed cross-flow mass flow rate and impingement jet flow rate from 0.2 to 0.4 could significantly reduce Nusselts number by a factor greater than 2.5.

Bruchez and Goldstein, 1975, experimentally studied the influence of cross flow on the heat transfer characteristic of partially confined and staggered impinging jets issuing from discrete round holes and slots respectively. For single or multiple jets, flow visualization results showed that the cross flow made the flow highly three-dimensional, which also increased the complexity of the flow structure and heat transfer situation. Huang et al., 1998, presented detailed heat transfer distributions for an array of in-line jets impinging on a plate with different cross flow orientations by employing a transient liquid crystal method. The different cross flow directions were created by changing the test section open ends. They reported that the highest heat transfer coefficients are obtained for a cross flow orientation where flow exits in both directions.

For the imposed cross flow case, Huang, Mujumdar, and Douglas, 1984 conducted a numerical investigation on the effect of the cross flow rate on the heat transfer performance under a turbulent impinging slot jet. They compared the predicted Nusselts number distribution including the effect of cross flow with those without cross flow. It was found that the location of the maximum Nusselts number shifted downstream due to the deflection of the jet by the cross flow. They further observed that the Nusselts

number far downstream from the slot exit for the case with imposed cross flow was higher than that without cross flow, which was in agreement with the Metzger, et al.'s, 1969 experimental observation on round jets in an imposed cross flow. The decrease of the Nusselts number over the downstream region was due to the total mass flow rate exhausted through downstream direction which increased as the cross-flow rate was increased. Galant and Martinez, 1982, presented a formulation of the cross flow influence upon impingement heat transfer rates for arrays of circular based on the jet height and diameter.   The formulation is shown below where Z=Height of the jet, D=Diameter of the jet, m= Cross flow to jet momentum ratio and ψ =Analytical Function of Z/D

$$\psi\left(\frac{Z}{D},m\right)=0.067\left(\frac{Z}{D}\right)^{-0.536}m^{-0.951} \longrightarrow \quad \text{Eq. 1.1}$$
$$Nu_x = 0.08\,\text{Re}_x$$

A study more relevant to the current situation was presented by Taslim and Setayeshgar, 2001, through a series of experiments of jet impingement on a leading edge wall with film holes. They studied circular and racetrack shaped impingement holes under both pure shower head and simulated tip flow condition. The jets in this study had a greater height (Z/D) than the jets used in the current study. Fig 1.7 shows the Nusselts number variation with respect to Jet Reynolds number for different flow configurations.

The 70 % showerhead case in Fig.1.7 refers to the flow configuration where 30 % of the flow exits through the tip while the rest exits through the film cooling holes. The current study is being conducted to obtain the heat transfer characteristics of a jet impingement system on a unique target surface geometry under different cross flow conditions and film cooling configurations.

8

1.3 Objectives and Outline of the Thesis

The current study involved a total of three stages. They are:

Task 1: Calculation of Coefficient of Discharge of the Impingement and the Film Cooling Holes (Chapter 2)
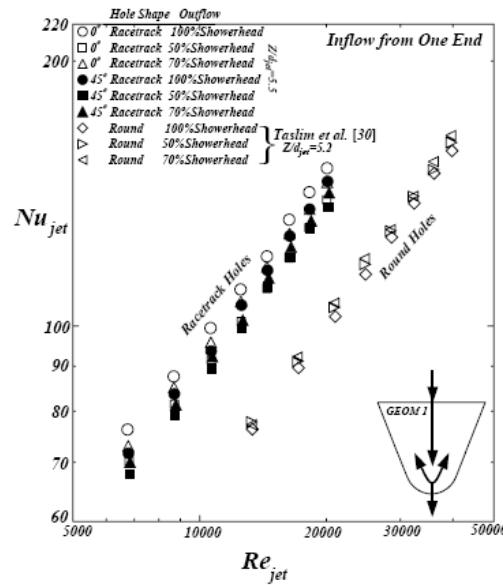
Fig 1.7: Comparison of results of racetrack shaped and round cross over jets
(Taslim and Setayeshgar, 2001)

Task 2: Benchmarking of the Camera-Endoscope technique against a Standard Camera-Lens Technique (Chapter 2)

Task 3: Liquid crystal based heat transfer tests on the internal cooling cavity surfaces under different impingement and cross flow conditions (Chapter 3)

The purpose of the first task is to obtain more information on the flow distribution within the test section under the given flow conditions. The discharge coefficient values are to be supplied to the Project Sponsor for the development of a flow model. The second task involved validation the novel image capturing technique being used in the current study by comparing it with a proven camera-lens technique. Heat transfer tests

were carried out on a rectangular channel using both the techniques and the results were compared. The third task involved obtaining the heat transfer contours for jet impingement under various configurations. The objective of these tests is to gain an understanding of the effect of different test parameters i.e. amount of cross flow, film cooling configuration and tip flow condition on the final heat transfer contour. The term cross flow in the present case refers to the existing spent flow from the upstream jets as well as an external cross flow provided in the radial direction. Each case had a different combination of the film cooling holes and hence there was a variation in the number of film holes available in each case. A variation of one of these cases was performed with a closed tip condition to obtain an understanding of the effect of tip condition on the heat transfer.

Chapter 2

Discharge Coefficients of Film Cooling Holes and Impingement Holes

2.1 Experimental Setup

The following sub sections describe the experimental set-up used in calculating the discharge coefficients.

2.1.1 Test Section and Flow Layout

The coolant flow from the supply tank is routed through a ball valve and a particulate filter to the flow circuit shown in Fig.2.1. The flow circuit consists of two branches: one leading to the impingement array and the other branch feeds the external cross flow plenum. At the inlet of each branch a Needle valve (Valve 2 and Valve 3 in Fig 2.1) is installed to adjust the flow rates in the respective branches. By adjusting these two valves, the flow rate through the test section can be conveniently controlled.

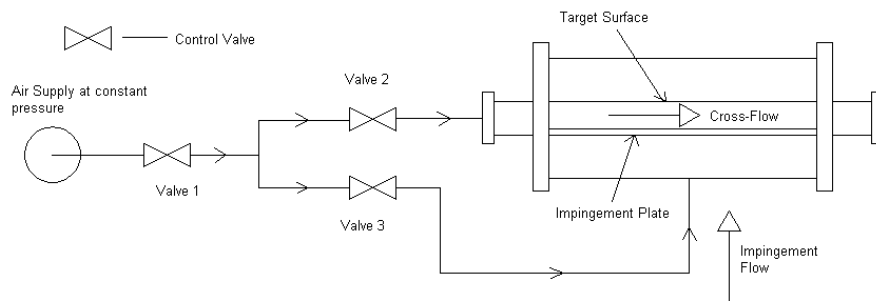Fig 2.1: Flow Circuit to that supplies air to the impingement plenum and the cross flow plenum

The Flow rates in the branches are monitored by two Omega FLR-D series, digital flow meters. The operating pressure is 100 psi and the operating range is 20 CFM-250 CFM. The air pressure at the inlet of these flow meters is obtained from an upstream pressure gauge and the flow is corrected for that value of the pressure.

11

The test section, in which the target plate and the impingement plate are housed, is made of perspex. It consists of the impingement plenum, peanut cavity and the outer chamber into which the peanut cavity discharges its flow. Figure 2.2 shows the cross section of the test section. The relevant chambers are labeled. The peanut cavity is encompassed by the target surface, the impingement plate and the support plate. The peanut cavity represents a scaled up model of the leading edge cavity of a turbine vane. The impingement cavity is made up of the impingement plate, the support plate and the external structure. The feed air from the air storage tank enters the impingement chamber and flows through the impingement holes into the peanut cavity where it strikes the target surface. The air from the peanut cavity sits through the film cooling holes into the external chamber which in turn exhausts the air into the atmosphere through two 2-inch holes. Figure 2.3 shows the solid model of the test section. The arrow in the figure indicates the cross flow direction. The tip exit of the peanut cavity is at the end pointed by the arrow. The target surface and impingement plate are described in detail in the sub sections.

2.1.2 Impingement Plate

The impingement plate is also constructed from Perspex. It has an inline row impingement holes. There are total of three sets of impingement holes with varying diameter. All the three sets and their arrangement are shown in Fig 2.4

2.1.3 Target Surface

The target surface is shown in Fig 2.5. It is constructed from Perspex and represents a section of the leading edge of a turbine vane. It has five rows of inclined film cooling holes of which the first four (Rows 1-4) represent the showerhead rows and fifth

12

row (row 5) represents the gill row. The impingement jets strike the target on inclined surface on which the row 4 is located. This represents the suction side of the leading edge cavity in a turbine vane. As evident from the geometry, the jet strikes the target surface at an angle of 30.5^0. The relevant dimensions are shown in the Fig. 3.6. A layer of black paint is sprayed on the inside of the target surface. Liquid crystal is then applied in the form of a fine spray on the black paint.
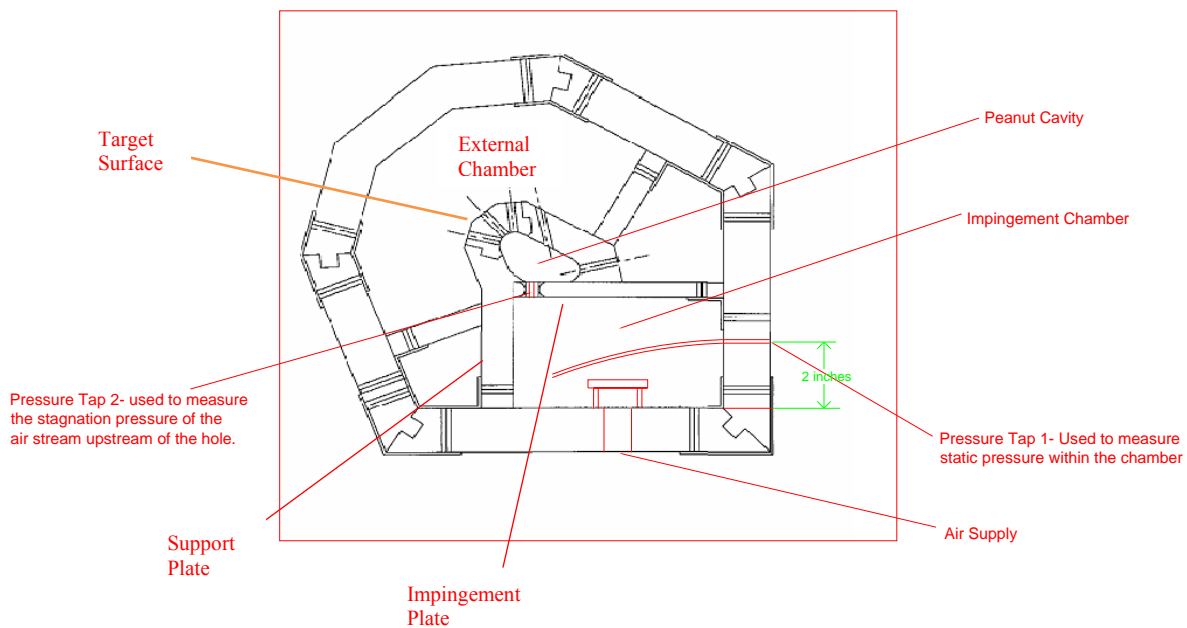
Fig 2.2: Cross Sectional view of the Test Section

2.1.4 Coolant Supply

The feed air to the impingement plate comes from a dedicated Atlas Copco GR 110 two-stage screw compressor. The air from the compressor is passed through a Pneumatech Inc. heatless, regenerative air dryer to remove any moisture that might be present in the supply. The pressurized, dry air from the drier is stored in a storage tank downstream. The purpose of the storage tank is to ensure a constant supply of dry air

13

without transmitting any supply pressure fluctuations due to the compressor cycle of operation.
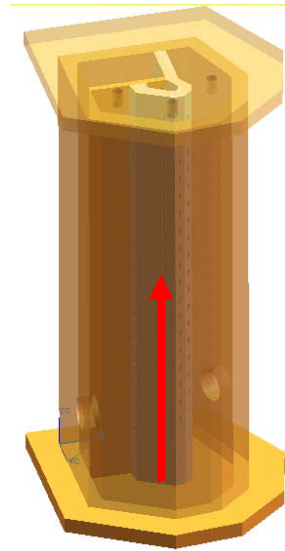
Fig 2.3: Solid Model of the Test Section
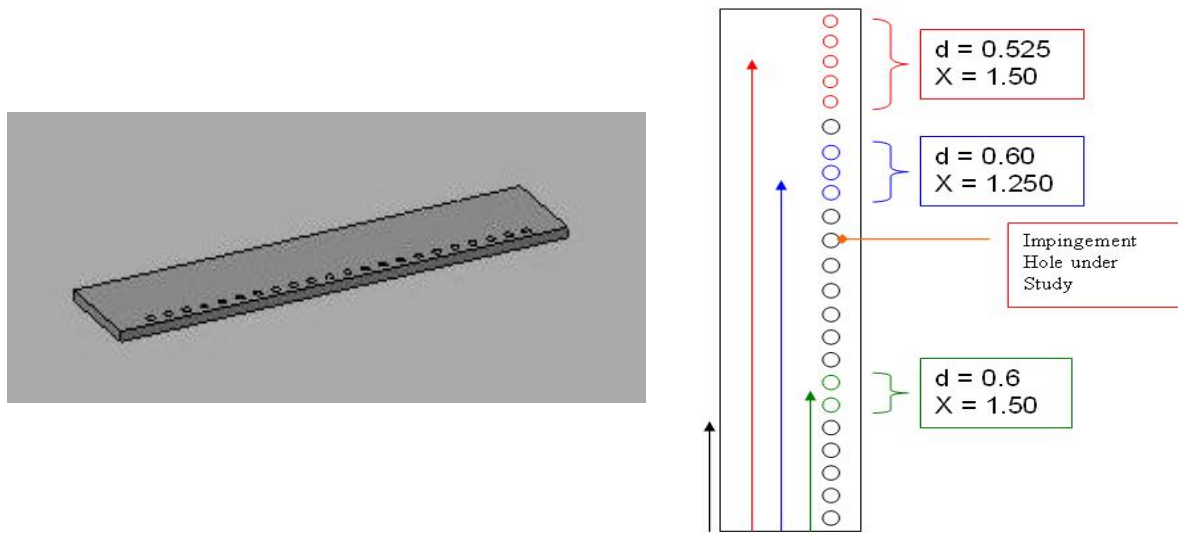
Fig 2.4: Impingement Plate and arrangement of the Impingement Holes
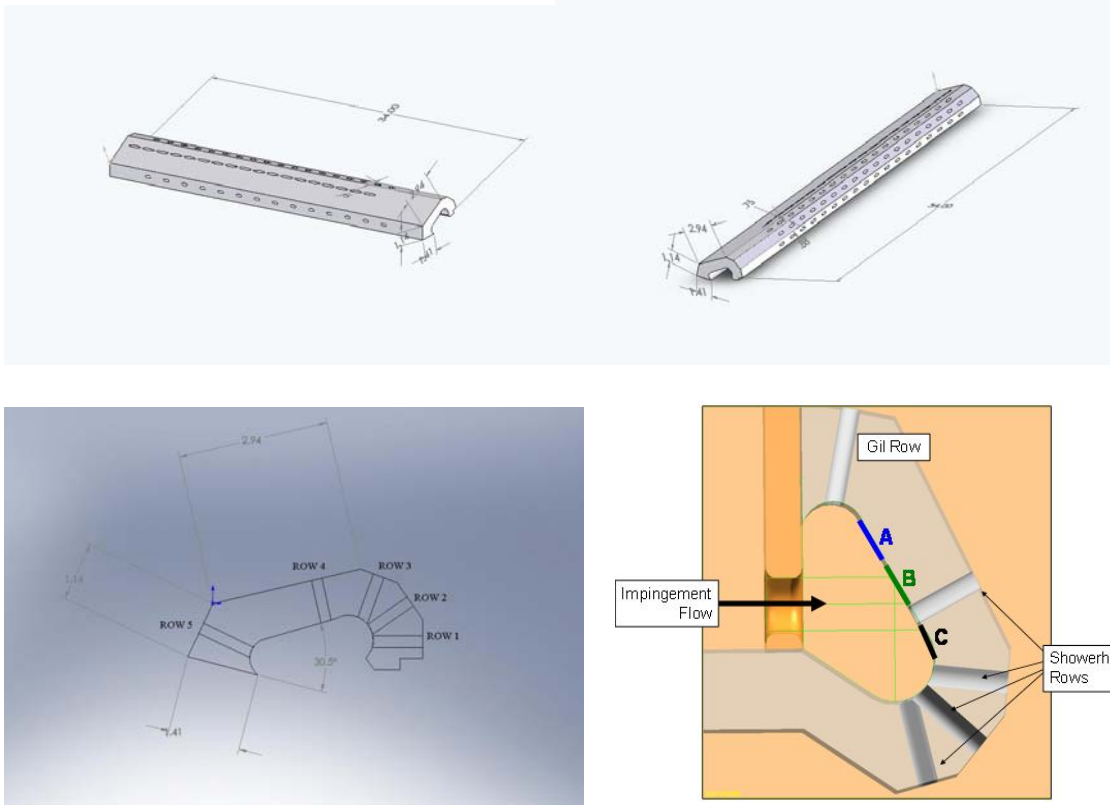
Fig 2.5: Target Surface

2.2 Flow Calculations- Coefficient of Discharge

The first stage of the project involved the measurements of the discharge coefficients of the Impingement Holes and Film Cooling Holes. This stage of the project was specifically carried out on the request of the sponsor in order for them to set up a flow model of the test rig based on the Discharge Coefficients furnished by the team at LSU. The flow model was computed using in-house software at Pratt and Whitney. The input parameters to this flow model were the pressure ratios across the impingement plate and the target plate along with the discharge coefficients of the holes. These parameters were used to set up a network flow model based on the principle of conservation of flow across all the sets of holes to compute the flow distribution across the Impingement plate and the

target surface. The sponsor then used the consequent flow distribution model as the basis to estimate the heat transfer coefficient distribution at the test location.

2.2.1 Procedure for Impingement Hole Cd Measurement

The discharge coefficients for the impingement holes are calculated by opening up the peanut cavity. This is achieved by removing the target surface from the top of the impingement plate and allowing the air to pass through the impingement holes into the outer plenum instead of the impingement cavity. A static pressure probe is then used to measure the pressure in the impingement plenum upstream of the impingement holes and the downstream pressure at the 'vena contracta' (cross section where the jet has the least diameter) of the jet. In case of the impingement holes, which have a contoured edge, the vena contracta is located exactly at the exit of the hole. These values of pressure are then used in the Bernoulli's equation to calculate the theoretical flow rate through the holes. The ratio of the observed flow rate (as obtained from the Flow Meter) and the calculated theoretical flow rate gives us the discharge coefficient of the hole. The experiment was repeated twice for each set of holes.

There are a total of twenty three impingement holes with three distinct groupings based on the diameter of the holes (D) and the pitch (distance between the holes i.e. X/D). This is shown in Fig 2.4 of the impingement plate. The discharge coefficients are calculated separately for each set of holes. When the flow test is being performed on one set of holes the others are closed using duct tape. This ensures minimal interference on the jets under test from the spent flow of jets from other holes. Figure 2.6 shows the variation of coefficient of discharge with varying flow rates. The two sets of data are

represented as 'run1' and 'run 2' in Fig 2.6. 'run 1' and 'run 2' refer to the consecutive sets of experiments performed on each set of holes under similar conditions.

It can be seen from Fig 2.6 that the discharge coefficients of the holes increases with increase in Reynolds number and tend to reach constant value at higher Reynolds numbers i.e. the coefficient of discharge increases as the flow increases but at higher flow rates the coefficient of discharge flattens out. The flow rate in the heat transfer tests is in the range of constant coefficient of discharge. A sample calculation of the discharge coefficient is shown below. The uncertainty in the calculated value of discharge coefficient is also shown.

Q_{Actual}= 70.1514 ft^3/min = 0.0331 m^3/s

P_1= Upstream Pressure = 1830 Pa

P_2= Downstream Pressure = 90 Pa

Y= Expansion Factor (~1)

d= Diameter of the hole = 0.525 in= 0.0133 m

A (5 holes in this case)=Total Area = $5 \times \dfrac{\pi d^2}{4}$ = 6.9831e-004 m^2

$Q_{Theoretical}$= $YA\sqrt{\dfrac{2(P_1 - P_2)}{\rho}}$ = 0.0362 m^3/s

C_d= $\dfrac{Q_{Actual}}{Q_{Theoreticall}}$ = **0.914**

The uncertainty in C_d is mainly due to the instrument error. Accuracy of the flow meter = $\pm 2\%$ of the full scale (Obtained from the manual provided). The pressure gauge was calibrated using a liquid manometer and was found to have no errors. Another 1% error is included to account for the fluctuations in the supply and

accuracy errors in the pressure gauge resolution. Therefore the uncertainty in the present study is concluded to be $\pm 3\%$. Also the test section used in the experimental set up, described in section 2.1.1 has a number of contact surfaces. These contact surfaces exist between the middle section of the body and the side plates and in the peanut cavity between the target surface, the support plate and the impingement plate. These contact surfaces are sealed using silicon sealant and adhesive cork tape. However, it was found form pressure readings for high pressure flow tests that there was some amount of leakage. It is surmised that this could be a result of some sections of the sealing buckling under the influence of the supply air pressure. This leakage effect adds to the uncertainty discussed above although the exact amount is difficult to determine.

2.2.2 Procedure for Film Cooling Hole Cd Measurement

The procedure used to measure the discharge coefficients of the film-cooling holes is similar to the procedure described above for the impingement holes. The downstream pressure for the film-cooling holes is the pressure measured at the vena contracta of the jet issuing from the film cooling hole. This pressure was measured using a pressure probe. However, the measurement of a representative downstream pressure for the film cooling hole presented a problem since there is pressure distribution within the peanut cavity. This is a result of the expansion of the jet flow leading to an increasing pressure profile downstream of the impingement jet. This pressure distribution is further affected by the presence of spent flow from the other jets situated upstream of the probe. Therefore for the purpose of calculation of discharge coefficients it was agreed by the team that the upstream pressure for the film cooling hole would be the static pressure
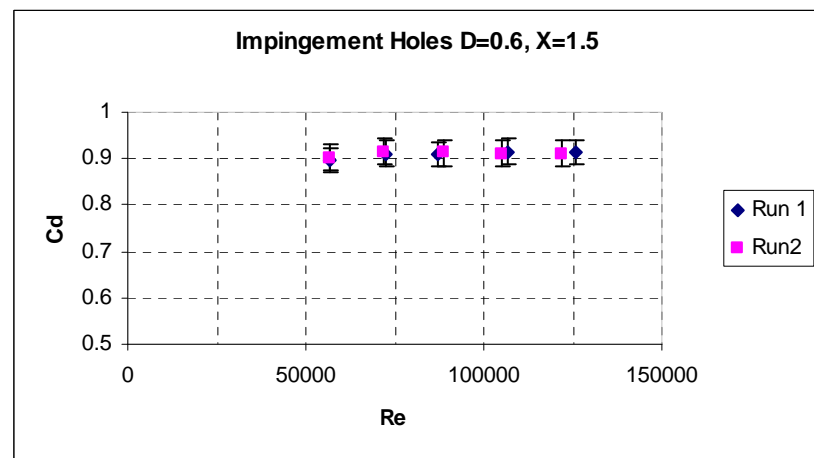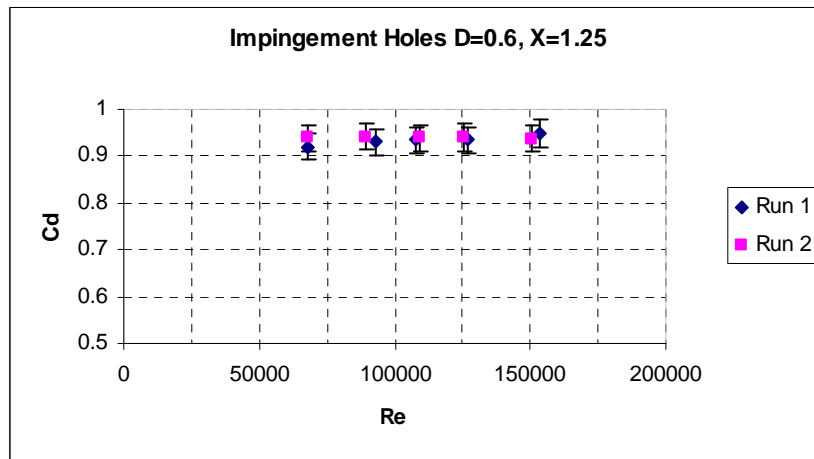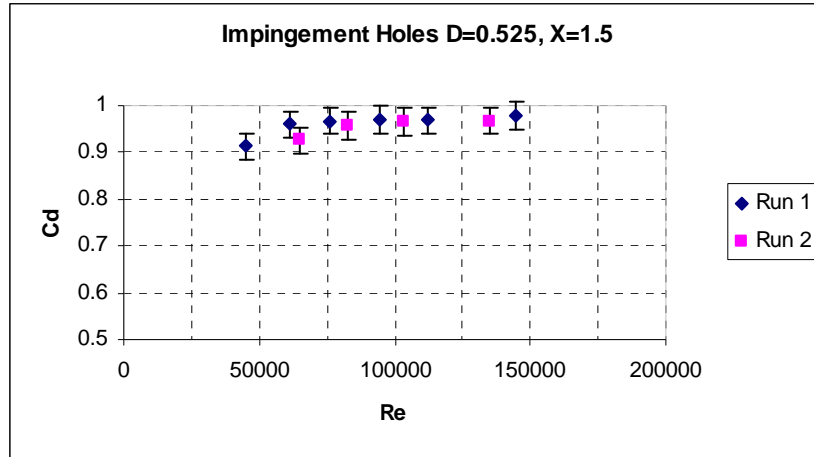
Fig 2.6: Variation of discharge coefficient with respect to flow rate for impingement holes, D=diameter of the hole, X=Pitch of the holes (Fig 2.4)

measured using a static pressure tap in the impingement plate. Subsequent to the measurement of the pressures (upstream and downstream) a formula based on the Bernoulli's principle was used to compute the theoretical flow through the film cooling holes. The coefficient of discharge was calculated as the ratio between this calculated flow and the observed flow corrected for the discharge coefficient of the impingement holes. Figure 2.7 shows the trend of coefficient of discharge with respect to flow rates for film cooling holes. 'Run1' and 'Run 2' in Fig 2.7 represent the data sets of the two runs of the experiment.

Fig 2.7: Variation of Coefficient of Discharge with Flow Rate for
Film Cooling Holes, Row Numbers correspond to those shown in Fig 2.5

20

Film Cooling Holes on the Gill Row (Row 5)

Chapter 3

Liquid Crystal Based Heat Transfer Tests

This chapter explains in detail the experimental setup used, the theory behind the experiment, procedure involved and the image processing technique used in the heat transfer tests.
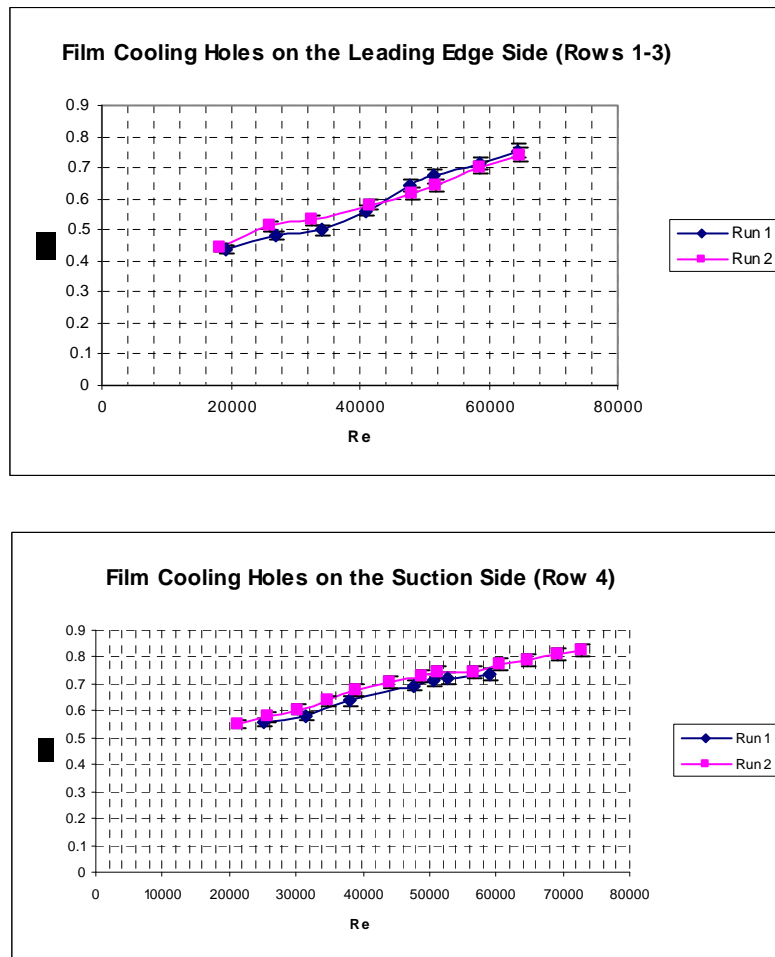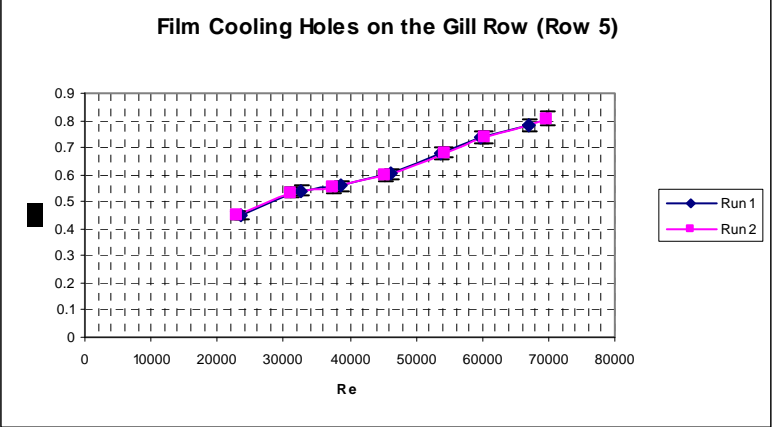
3.1 Experimental Setup

The experimental set up consists of all the apparatus described in section 2.1. The additional components used in the experimental set up for the heat transfer tests are described in the sub sections below.

3.1.1 Temperature Measurement

The temperature of the feed air to the impingement plenum and the surface temperature of the target plate are continuously monitored using K-type thermocouples. A total of seven thermocouples were positioned at 10%, 50% and 90% span wise locations on the target surface to monitor the surface temperature. The thermocouples were calibrated using a digital calibration meter. An Omega DMB seven channel, digital data acquisition board was used to log the data from the thermocouples.

3.1.2 Heating Arrangement

A heater-blower combination is used to supply the hot air required to heat the target surface. The heater is an inline coil-based heater with a power rating of 1000 W. The target surface is heated by running the hot air from the heater blower combination through the peanut cavity till the required test temperature is attained. Then the heater-blower combination is disconnected from the flow circuit.

3.1.3 CCD-Camera and Endoscope

The liquid crystal images are captured using a Camera-Endoscope combination. The camera used in the current studies is a Pulinx CCD camera capable of recording 30 frames per second. The endoscope is essentially an industrial boroscope manufactured by ITI technology. The endoscope has a special attachment which allows it to be coupled to the lens of the CCD camera. There is a fiber optic cable within the stem of the endoscope which transmits the optical images from the endoscope lens to the camera lens. A sleeve equipped with a 45^0 mirror is also provided with the endoscope. By sliding the sleeve over the endoscope, the target surface can be viewed at right angles. Figure 3.1 shows the endoscope and the accompanying sleeve with the mirror

Fig 3.1: Endoscope and Accessory Sleeve

The illumination for the image was provided using a graduated halogen light source connected directly to the endoscope. This light source is customized for use with the endoscope and is manufactured by ITI. The images from the Camera are directly uploaded to the computer using an on-board frame grabber card PCI 1400.

3.2 Thermochromic Liquid Crystal Technique

Thermochromic Liquid Crystal (TLC) can be bought commercially in micro-encapsulated form and in the work reported here it is spray-painted onto the target

surface. The crystals display color from blue to green to yellow as the surface temperature cools from a temperature above the high threshold level (or in reverse if the surface is heated from below the lower threshold temperature). Above this upper threshold and below the lower threshold level, the TLC is clear. TLC is available with either a wide or narrow band of temperature during which the color play is visible. Narrow band TLC can be used to measure the surface temperature to an accuracy of about 0.1 °C and can be used to locate a particular temperature isotherm at a particular color, hue or intensity value. Multiple narrow band crystals can be used to identify multiple isotherms, and the surface temperature at a particular time can be recorded by recording the color play of the crystals. Wide band TLC are implemented if a continuous variation in temperature with time is required, as the color play is over a significantly larger temperature range and the full color play is used to measure the temperature variation over 20°C.

In addition to providing temperature traces at points on the surface of the turbine vane, the TLC images are an effective flow visualization tool. The flow through the vane cavity can be found to be skewed toward the leading edge

For the current studies a narrow band liquid crystal in the temperature range of 39.5-40.5 degrees centigrade has been employed. The liquid crystal was calibrated and the calibration curve of hue variation with temperature is shown in the Fig 3.2. The threshold hue value for processing the liquid crystal images was chosen at 39.5^0C.
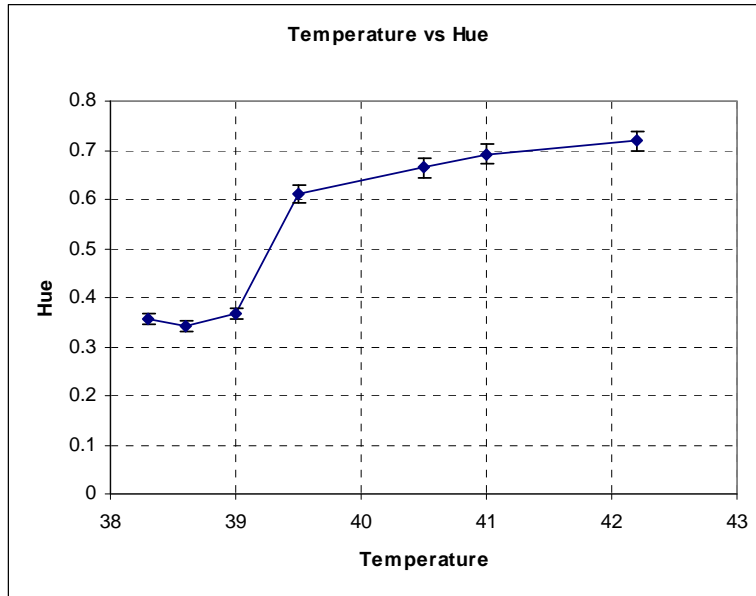
Fig 3.2: Calibration curve for the Liquid Crystal

3.3 Benchmarking of the Camera-Endoscope Combination

The second stage of the project involved validating the CCD Camera- Endoscope technique against a standard, proven technique. The benchmark test used in this case involved the measurement of heat transfer coefficients on the wall of a rectangular channel using a CCD Camera-Lens combination. The Camera-Lens technique is a proven technique that has been used extensively in previous studies involving the derivation of heat transfer profile using Thermochromic liquid crystal. This phase was mandated since the Camera-Endoscope technique was being used for the first time in a liquid crystal based heat transfer test. The experimental rig for this test is shown in Fig 3.3 below.

The setup for this phase includes a

- 4:1 aspect ratio channel with heating elements in the walls. Hydraulic Diameter=21.875 mm

- Liquid crystal sheets inserted behind the heating element

- Liquid Crystal spray (described in Section 3.2) on the channel (inner) surface of the wall

- Kapton sheet

- K-type Thermocouple

- CCD camera

- Adjustable Lens

- Endoscope

- Light source

- Power supply for the heating elements
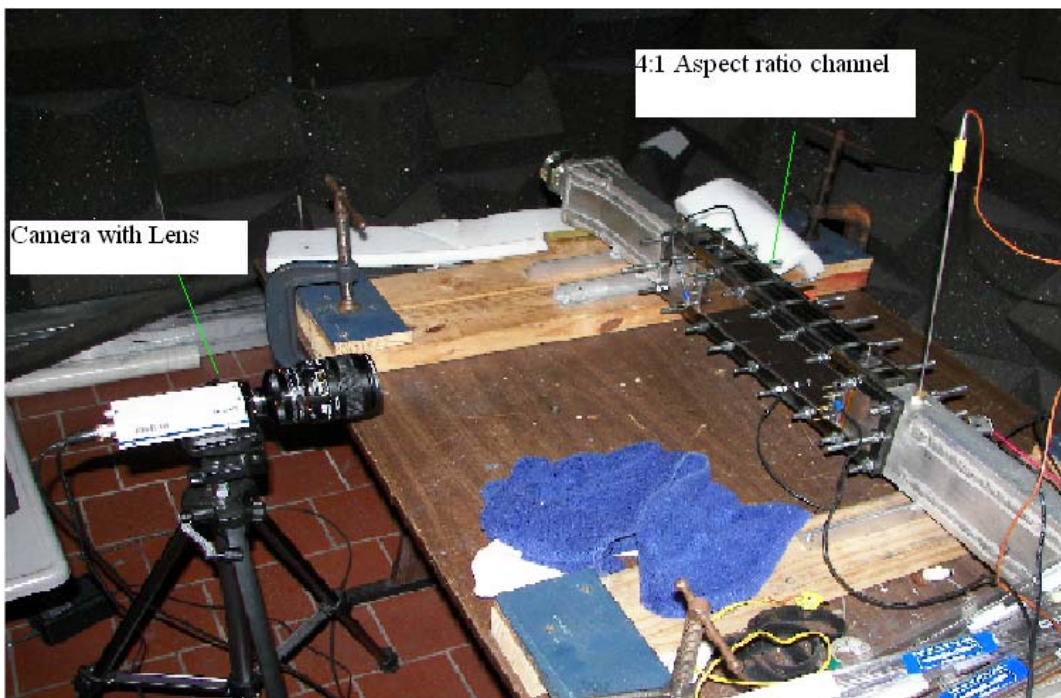
- Air Supply

Fig 3.3: Experimental Setup for Benchmarking the Camera-Endoscope combination

The Rectangular Channel was constructed using four separate Perspex walls which can be combined between two rectangular, steel pipe sections to form the channel. A

series of specially designed double ended threaded screws are used to connect the plates with each other and with the cast iron pipe sections. The heating elements are embedded in all the walls and are exposed to the coolant air flowing in the channel through a thin Kapton sheet. The Channel is supplied with coolant air from one end through a metal pipe. The other end is left open to the atmosphere. The coolant air is sourced from a compressor (Characteristics specified in section 2.1.4) capable of supplying air at a constant pressure. The flow rate is maintained constant by employing a throttle valve upstream of the channel. The liquid crystal sheets used in the channel walls are located behind the heating elements. The liquid crystal spray is sprayed on the Kapton sheet attached to the inner surface of the channel wall. Both varieties of liquid crystal have been calibrated separately. The heating elements are connected in parallel to a pair of terminals. The power source for the heating elements is connected to these terminals. The CCD Camera and the endoscope used in this test are the same as the ones used in the actual heat transfer tests in section 3.1.3. A Nikon Nikkor AF-SVR DX adjustable, high resolution, aspheric zoom lens was used in the camera Lens combination. Fig 3.3 shows the camera-lens combination. The light source used in both the cases is also the same (Section 3.1.3).

3.3.1 Experimental Procedure and Results

The heating elements were connected to the power source and the power setting is adjusted to obtain a predetermined temperature on the channel wall. The wall temperature is continuously monitored using a K-type thermocouple placed on the channel side of the wall. The procedure involves the following steps:

- The air is supplied from the source at a constant rate. The calculated Reynolds number of the flow is Re = 74423.65

- The power source to heating elements is adjusted such that a steady temperature profile is reached throughout the walls of the channel. This involves getting a steady color distribution in liquid crystal sheet.

- A specific area- $X/D_h = 6.9$ ($X=$ Axial Distance from the entrance, $D_h=$ Hydraulic Diameter of the channel $=21.9$mm) is chosen in the wall and the camera –in both combinations- is focused onto this area. The camera-lens combination focuses on the liquid crystal sheet visible from the outside while the endoscope focuses on the liquid crystal spray on the Kapton sheet located on the inner surface of the channel wall. The light source used in both the cases is the endoscope light source. A set of Liquid crystal Images obtained from both the combinations is shown below

The dimensions of the area covered by Camera-Lens combination is 1.5 inches x 1.125 inches, whereas, the Camera-Endoscope captures a circular area of Diameter 0.75 inches. The relevant area has been indicated by a circle in the first liquid crystal image captured by the Camera-Lens combination in Fig 3.4. Subsequently these images are processed (described in Section 3.5) and the area averaged heat transfer coefficients are compared.

The calculated values of average Heat Transfer Coefficients (HTC) for both the cases are plotted against the temperature difference between the coolant flow and the heated wall in Fig 3.5 below. Figure 3.6 shows a plot of Nusselts number variation with increasing temperature for both the cases and both the cases are compared with values

calculated from the Dittus-Boelter equation. A good agreement is found between the results obtained using both the combinations i.e. Camera-Lens and Camera-Endoscope. The

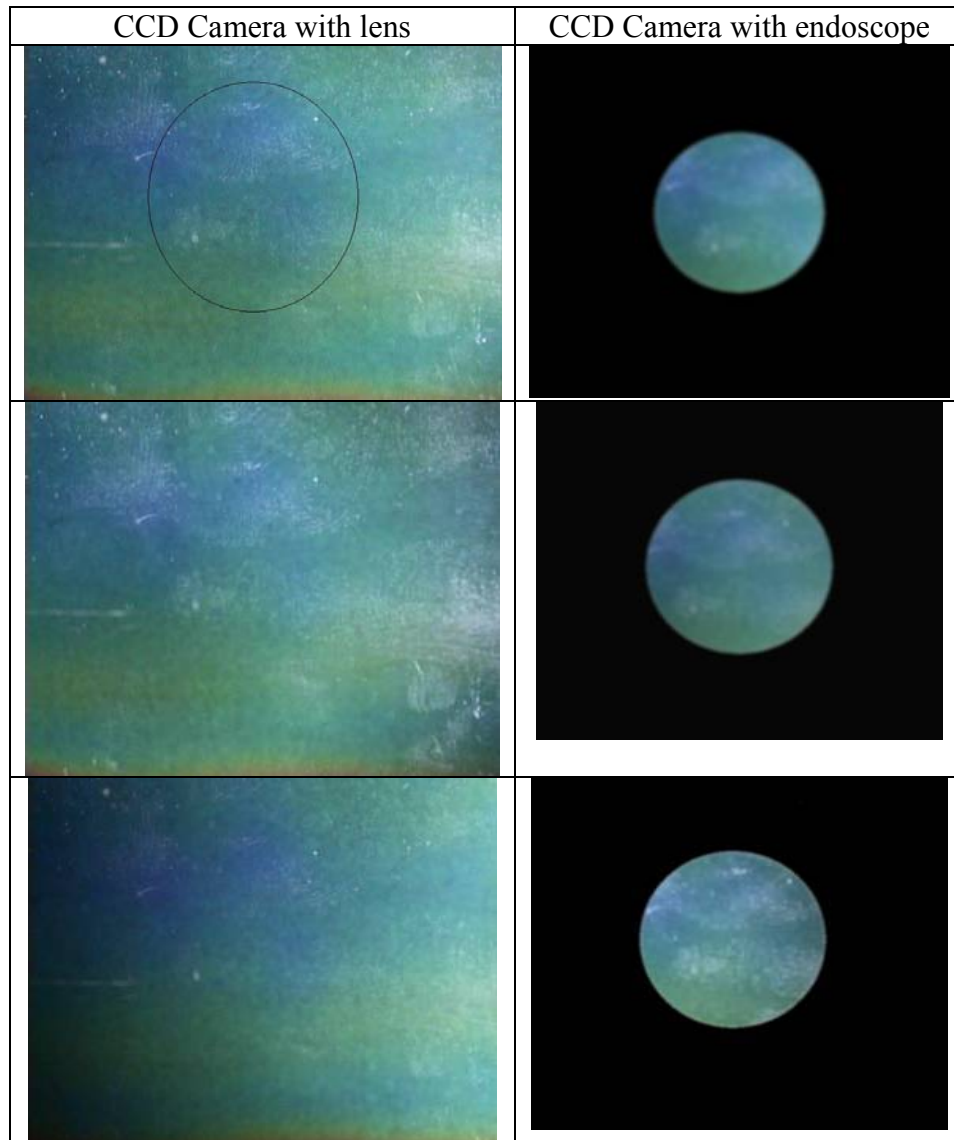| CCD Camera with lens	CCD Camera with endoscope

Fig 3.4.: Comparison of liquid crystal images captured by the Camera-Lens and the Camera-Endoscope combination.

benchmark tests provide a validation for further usage of the Camera-Endoscope technique.
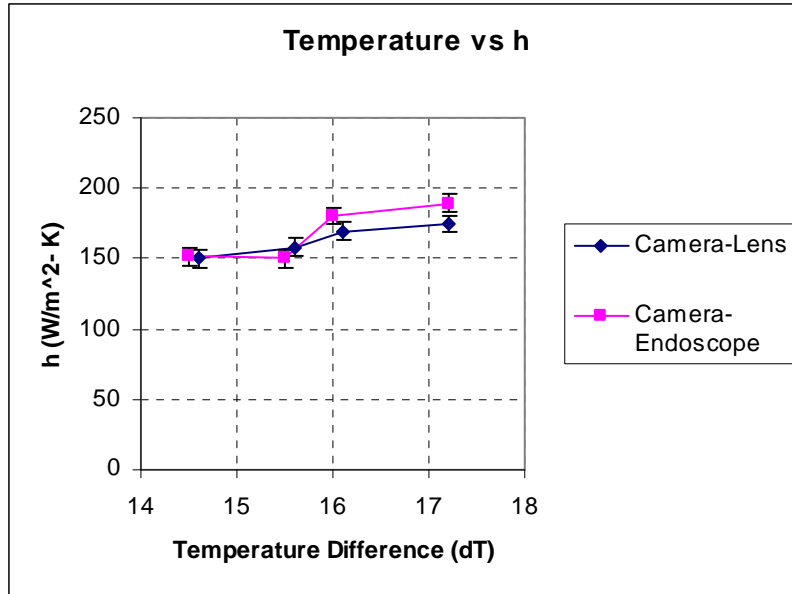
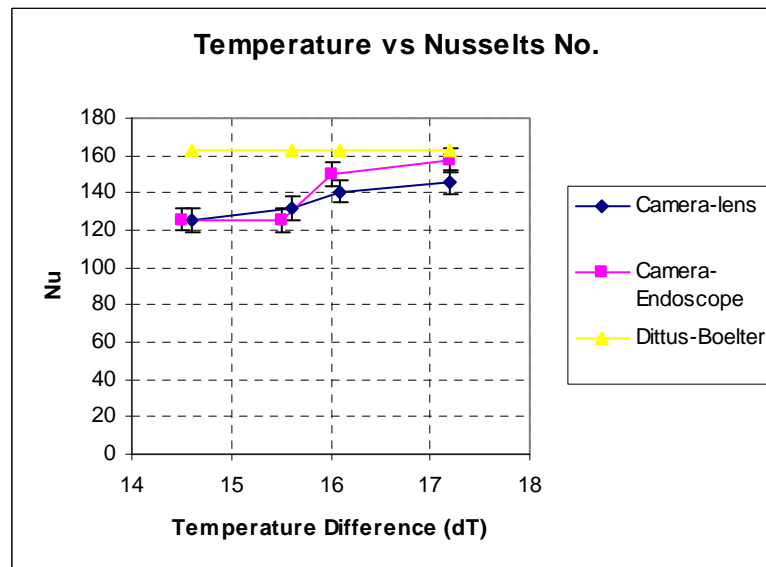Fig 3.5: Variation of Heat Transfer Coefficient (HTC) with respect to Temperature Difference

Fig 3.6: Variation of Nusselts number with respect to Temperature Difference

A sample calculation of all the values shown in the plots is given below. Also the uncertainty in the calculated values of heat transfer coefficient and Nusselts number is given. The calculated uncertainty is shown as the error bars for each value in the plots.

Thermocouple Temperature, TTC= 39.5^0C

Flow rate= 71.15 CFM= 0.03358 m^3/s

Power input, q= 38 W

Area= 0.0155 m^2

Kinematic Viscosity= 1.41e-5

Hydraulic Diameter of the Rectangular Channel, D_h= 0.021875 m

Flow Reynolds Number, Re_{Dh}= 74423.65

Prandtl Number= 0.70

Thickness of the Kapton Sheet, dx = 0.0001 m

Thermal Conductivity of the Air, K= 0.0263 W/m-K

Temperature on the Liquid Crystal= 39.5+ ((q/Area)*dx/K) = 40.2^0C

Temperature Difference, dT = 40.2-24.9= 15.3

Heat Transfer Coefficient, h=q/ (Area*dT) =145.0114

Nusselts Number= 145.0114*0.021875/0.0263= 120.6131

Dittus-Boelter Correlation= 0.023*Re^(0.8)*Pr^(0.3)= 163.1635

Uncertainty for Heat Transfer Coefficient, h:

Uncertainty in the thermocouple reading= $\pm 0.5^0$C

If T=39, Nu=149.9685 => Error=3.42%

If T=40, Nu=140.3716 => Error=3. 20%

Adding another 3% to account for the uncertainty in instrumentation, we have,

Total error on either side would be 6.42% to 6.2%

3.4 Theory and Mathematical Formulation

The target surface is modeled as a semi-infinitely thick slab subjected to transient

heat transfer. This means that the target surface is affected by the coolant flow at the exposed end only while the other end is not affected by the boundary condition at the exposed end i.e. the penetration depth of the cooling effect is low and confined to the exposed end only. Penetration depth of a medium is dependent upon the thermal diffusivity (α) and the duration of the test (t). Equation 3.1 defines the penetration depth quantitatively

$$\text{Penetration Depth} = \sqrt{\alpha t} \qquad \text{Eqn 3.1}$$

The target surface is made of 1-inch thick perspex. Perspex has a low thermal diffusivity value. Thermal diffusivity for perspex is equal to 1.099 x 10^{-7} m^2/s and, the maximum duration of heat transfer test in any configuration is only 15 Seconds. Substituting in the formula for penetration depth we obtain a value of .0013 m or 0.051 in which is much lesser than the thickness of the plate. Therefore the semi-infinite slab assumption for the target surface is valid. Fig 3.7 below shows the schematic of convective heat transfer over a semi-infinite slab.
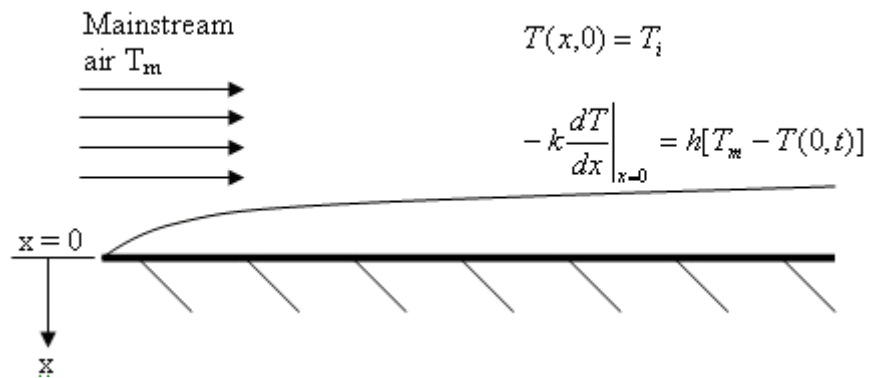

Figure 3.7: Heat Transfer over a Semi Infinite Slab [3]

The slab is initially at a uniform temperature T_i at time, t = 0. At time t>0, the slab is suddenly exposed to a stream of hot air of temperature T_m. The hot stream of air

provides a heat flux to the surface of the slab and convective heat transfer phenomenon occurs. Balancing thermal energy in the surface of the slab yields the following equation,

$$\left(\frac{\partial^2 T}{\partial x^2} + \frac{\partial^2 T}{\partial y^2}\right) = \frac{1}{\alpha}\frac{\partial T}{\partial t} \qquad \text{Eq 3.2}$$

Subject to the following conditions,

$$T = T_i \text{ at } t = 0 \qquad \text{Eq 3.3}$$

$$-k\frac{\partial T}{\partial x} = h(T_w - T_m) \text{ at } x = 0 \text{ and } t \geq 0 \qquad \text{Eq 3.4}$$

$$T = T_i \text{ at } x = \infty \text{ and } t \geq 0 \qquad \text{Eq 3.5}$$

Where

T_w = Test surface wall temperature

T_i = Test surface initial temperature

T_m = Mainstream air temperature

k = Thermal conductivity of test plate material

α = Thermal diffusivity of test plate material

t = Time span for which hot mainstream air is blown

h = Heat transfer coefficient

Equation 3.3 represents the initial condition of the target surface. Equation 3.4 represents the convection boundary condition at $x = 0$. Equation 3.5 represents the second boundary condition at $x = \infty$ i.e. the unaffected end of the target plate. Further since the penetration depth is small, the lateral temperature gradient (y-direction) will be small. Hence equation 3.2 can be reduced to the following one-dimensional form

$$\frac{\partial^2 T}{\partial x^2} = \frac{1}{\alpha}\frac{\partial T}{\partial t} \qquad \text{Eqn 3.6}$$

The solution of the problem comprised of equations 3.6, 3.3, 3.4 and 3.5 is of the following form

$$\frac{T_w - T_i}{T_m - T_i} = 1 - \exp\left(\frac{h^2 \alpha t}{k^2}\right) erfc\left(\frac{h\sqrt{\alpha t}}{k}\right) \quad \text{Eq 3.7}$$

In Equation 3.7 all the material properties are known and the temperatures T_i and T_m are measured by the thermocouples. The surface temperature T_w at different time instances t is obtained from the heat transfer tests. Thus heat transfer coefficient h can be calculated.

3.5 Experimental Procedure

The endoscope is positioned at the test site in the peanut cavity and properly focused to obtain a clear image. Then heater-blower combination is used to heat the target surface to the required test temperature. The combination of heater blower is plugged to one end of the test section and the heated air from the blower is circulated through the peanut cavity. The heater-blower combination is run alternately from both ends of the test section so that a fairly uniform temperature distribution may be obtained in the stream-wise direction. Then the combination is switched off and disconnected from the setup. The temperature of the target surface is continuously monitored by the thermocouples placed on its surface. Before starting the actual heat transfer test acquisition and storage of the target surface temperature in real time is started. After the test section has acquired the test temperature, the frame grabbing software on the computer is activated to start recording images of the liquid crystal in the peanut cavity at a predetermined frame rate. Subsequently, coolant flow to the impingement plenum is begun. The test is continued till the liquid crystal has passed through its calibrated temperature range and is completely decolorized.

3.6 Post Processing of Liquid Crystal Images

The liquid crystal images obtained from the heat transfer test are processed to extract the heat transfer contours. A MATLAB program has been developed to process the set of images and superimpose the heat transfer information from all the frames onto a single frame thus providing a detailed distribution of heat transfer coefficients. The MATLAB code essentially solves equation 3.7 of section 3.4 for different time instances and stores these values in an array. Then an image filter is applied to each of the frames to isolate all the pixels that exhibit the threshold hue value corresponding to the one degree transition band of the liquid crystal. This threshold hue value is obtained from the calibration chart shown in Fig 3.2. The isolated pixel values in each frame represents an isotherm i.e. all the points that are at the same temperature. All the isotherms thus obtained are superimposed onto a single frame and are assigned the respective heat transfer coefficient value from the previously stored array using the time instance of the frame as a reference. A sample liquid crystal image and the final superimposed heat transfer contour is shown in Fig 3.8. The color of each pixel corresponds to a heat transfer coefficient value based on the color scale shown beside the figure. For example, in Fig 3.8 the impingement zone lies in the color scale between 250 W/m^2-K and 300 W/m^2-K.

This heat transfer contour is in the camera view i.e. the pixel coordinates are skewed in a perspective view and are do not represent the true physical dimensions of the target Surface. Hence this image has to be transformed to coordinates that represent the target surface as viewed by the endoscope lens when placed parallel to it i.e. the top view. The procedure for obtaining the top view is based on using the reference image (Fig 3.11)

to create a grid based on the actual geometric location for the area of interest. The reference image is that of a grid placed over the target surface at the exact location where the actual heat transfer test was conducted. The highlighted points on the grid are used as nodes. All the physical dimensions of the grid shown are in advance.
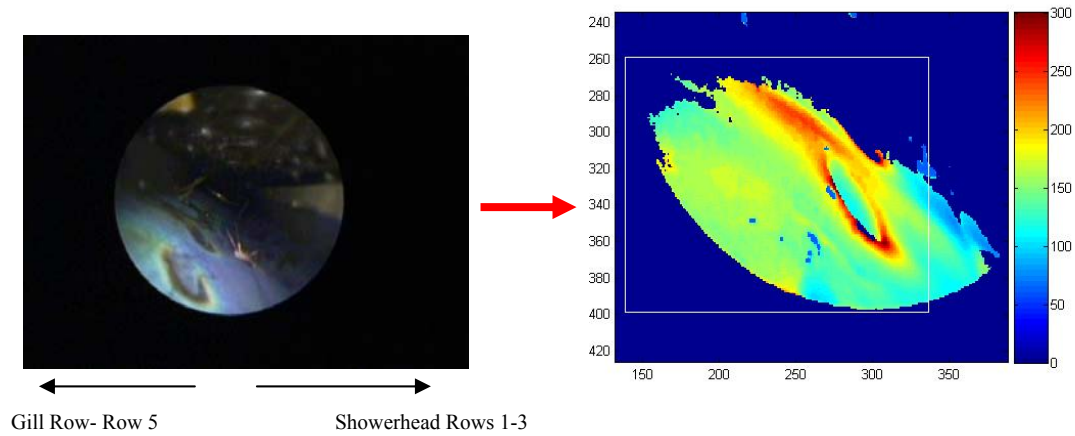

Gill Row- Row 5   Showerhead Rows 1-3

Fig 3.8: Transformation of Liquid crystal image into a heat transfer contour

Since both the physical location and camera-view coordinates for the nodes are known, this information is used as reference to find a one-to-one mapping between the pixels from the images in camera view to the top view. The required interpolation of the final pixel coordinates is performed using the 'griddata' method in MATLAB. The area of interest in the heat transfer contour image is represented by the white box in Fig 3.8. Figure 3.10 and Fig 3.11 show the plot of final coordinates of pixel in the top view and the transformed image respectively.
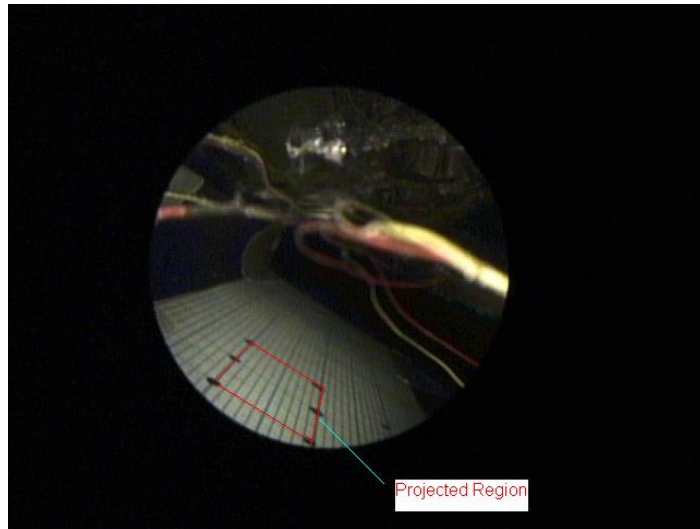
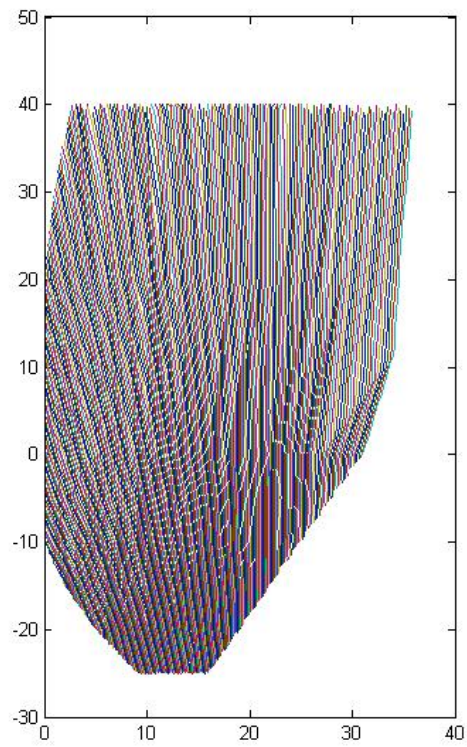Fig 3.9: Physical Grid on the target surface

Fig 3.10: Plot of the final coordinates of the pixels in the top view, the plot coordinates
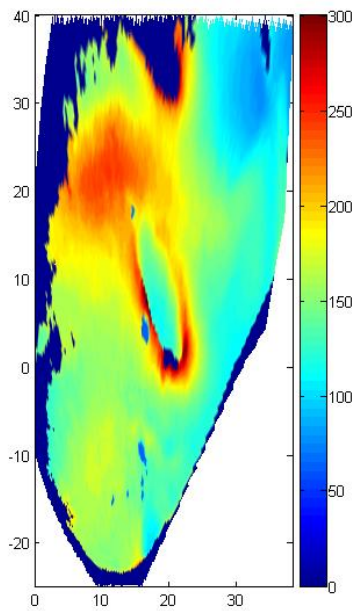indicate the physical location of each pixel

Fig 3.11: Top view of the Heat Transfer Contour showing the values of heat transfer coefficient in W/m^2-K. Color to heat transfer coefficient correlation is shown in the color scale from 0-300 W/m^2-K

Chapter 4

Heat Transfer Results and Discussion

4.1 Heat Transfer Results

Five different film cooling rows configurations have been tested. All five cases have the tip of the peanut cavity open to a plenum which in turn is exposed to the atmosphere. A sixth case, which has the same film cooling hole configuration as the first case but with tip closed has also been performed. The measured jet Reynolds number (Re_{jet}) based on the jet diameter for each of the cases lies within the range of 26000 to 26700. Two different ratios of external cross flow are also tested for all six cases. They are $0.25Re_{jet}$ and $0.5Re_{jet}$ i.e. the ratio of the cross flow Reynolds number to the Jet Reynolds number are 0.25 and 0.5 respectively. The cross flow Reynolds numbers are based on the hydraulic diameter of the peanut cavity. The matrix in Table 4.1 clearly shows the configuration of parameters used in each of the cases. Row numbers are based on the numbering system used in Fig 3.6 of the target surface.

Table 4.1 - Table of the Test Matrix, Row 1-5 are represented in Fig 3.6

	Row 1	Row 2	Row 3	Row 4	Row 5	Tip
Case 1	**Open**	**Open**	**Open**	**Open**	**Open**	**Open**
Case 2	**Open**	**Open**	**Open**	**Open**	**Open**	**Closed**
Case 3	**Open**	**Open**	**Open**	**Open**	**Closed**	**Open**
Case 4	**Open**	**Open**	**Open**	**Closed**	**Open**	**Open**
Case 5	**Closed**	**Closed**	**Closed**	**Closed**	**Open**	**Open**
Case 6	**Closed**	**Closed**	**Closed**	**Closed**	**Closed**	**Open**

4.1.1 Heat Transfer Contours

Cases 1, 2, 3, 4, 5 and 6 show the heat transfer contours for the six different configurations used. For each of the cases the first column shows the heat transfer contour as seen in the field of view of the endoscope and the second column shows the same contour after it has been transformed into the orthogonal or top view. The heat transfer contours represent the value of heat transfer coefficient h at each pixel in W/m^{2}K. Each Case is followed by a line plot which maps the heat transfer coefficient against the stream wise location (from the top view of the contour). The line along which each plot has been made is the line that passes through the point of maximum heat transfer (PMHT) encompassing all the pixels from stream wise location -25 to 30. The direction of the cross flow is from the positive coordinate to the negative coordinate of the stream wise location indicated by an arrow in Fig 4.2.

In Case 1, where all the film cooling rows are open we see two distinct impingement regions with two distinct peaks. Since all the film holes are open a greater part of the spent flow exits through the film cooling holes than through the open tip. The amount of flow leaving the peanut cavity through the tip is 30% and the rest exits through the film cooling holes. In Case 1(ii) and Case 1(iii) there is a significant drop in heat transfer in the impingement region owing to enhanced cross flow resistance encountered by the impinging jet. Also the impingement zone has shifted downstream under greater deflecting force from the increased cross flow. This is clearly illustrated in the line plot in Fig 4.2. Also the upstream peak of all the line plots is greater than the downstream peak clearly illustrating the effect of spent flow of the upstream jet on the downstream jet. In all three instances of Case 1 there is a decline in heat transfer as we move away from the

impingement zone. However more uniform heat transfer profiles are observed in Case 1(ii) and Case 1(iii) than Case 1(i).

Case 2 is a variation of Case 1 in that the tip of the peanut cavity is closed during the test. The entire cross flow exits through the film cooling holes. Therefore there is no spent flow effect in this case. However just as in previous cases the line plot in Fig 4.3 shows a reduction the downstream peak compared to the upstream peak. This can be attributed to the presence of jet to jet interaction. Compared to the previous cases there is lower cross flow effect on the downstream jet and therefore the jets spreads in a uniform circular fashion leading to an interaction between the spreading zones. In all the previous cases the cross flow reduces the possibility of any such interaction. Although this case exhibits the highest peak heat transfer coefficient compared to any of the previous cases, the impingement zone has a much reduced area. This is mainly because the impingement zone exists directly on top of the film cooling hole thereby reducing the effectiveness of the jet. Unlike any of the previous case, the heat transfer contours for all three instances of Case 2 exhibit similar heat transfer profiles and have nearly identical peak heat transfer coefficients. This similarity indicates that the externally supplied cross flow has minimal effect on the jet and is being routed through the film cooling holes upstream of the field of view. Hence the impingement jets in the field of view are devoid of any influence by external cross flow.

For Case 3, the number film cooling holes available for the cross flow to exit are lesser compared to Case 1 since the gill row is closed. Therefore there is more cross flow exiting through the tip than through the film cooling holes leading to a reduction in the magnitude of the peak heat transfer coefficient from 276.4 W/m^{2}K to 256.7 W/m^{2}K.
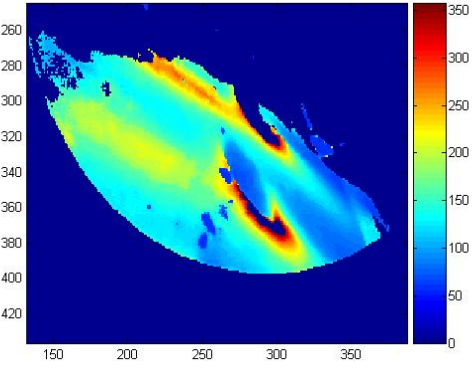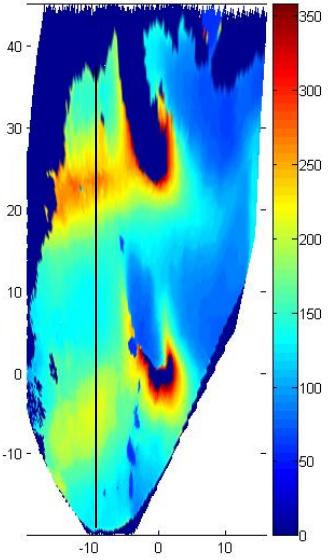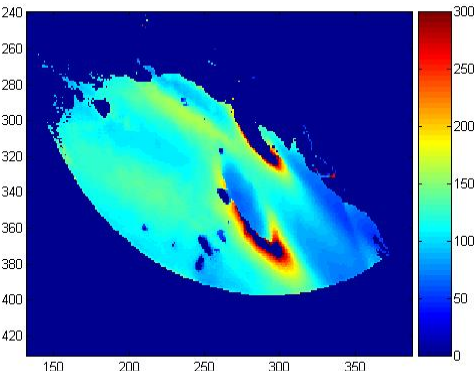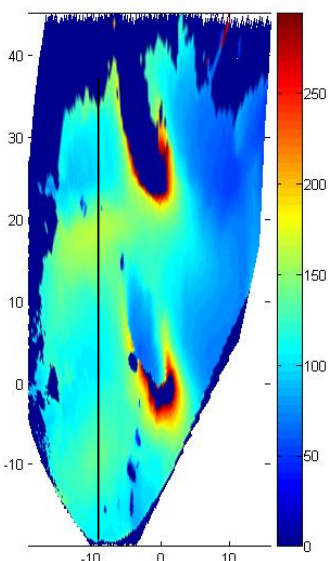
There is an associated improvement in the heat transfer away from the impingement region as the magnitude of cross flow has increased. When we compare line plots for Case 1(ii) and Case 1(iii) with the plots for Case 3(ii) and 3(iii) we observe a slight increase in the peak heat transfer coefficient and also an associated increase in the value of the heat transfer coefficients away from the peak. A more uniform heat transfer profile is observed for all three instances. This is also evident in the line plot in Fig 4.4 where the slope of the peak is less steeper compared to Fig 4.2.

In Case 4 we have configuration similar to Case 3, but for the location of the open rows of film cooling rows. Row 4, which is the row directly in the impingement zone, is kept closed. Compared to Case 1(i) we see a 10 % increase in the value of peak heat transfer coefficient in case 4(i). Also the impingement zone in Case 4(ii) is markedly improved compared to the corresponding previous instances. The major difference that can be observed between the present case and Case 3 is the improvement in the heat transfer performance in the regions away from the impingement zones. The line plot in Fig 4.5 also shows a lesser slope than witnessed in Case 1 indicating a more uniform profile.

In Case 5 there is drastic reduction in the number of film cooling holes open compared to the previous cases. Majority of the cross flow exits through the open tip. The heat transfer contour for Case 5(i) is much more uniform than the corresponding instances the previous cases as we move away from the jet. The peak heat transfer for Case 5(i) stands at 257.6 W/m^{2}K which is comparable to the results in Case 3(i). Case 5(ii) and Case 5(iii) witness a 15 % drop in the peak heat transfer compared to similar

instances in previous cases and exhibit only barely discernible peaks in the line plot in Fig 4.6.

Table 4.2 - Case 1: Rows 1-5 are Open, Tip is also open

Heat transfer contour, camera view	Processed Heat Transfer Contour (h W/m^2-K)
(i) Pure Impingement Flow, Re_{jet} = 26059	
(ii) Impingement +Cross Flow $Re_{cross-flow}/Re_{jet}$=0.25	

(Table contd.)

43

(iii)

Impingement +Cross Flow
$Re_{cross-flow}/Re_{jet}$ =0.5
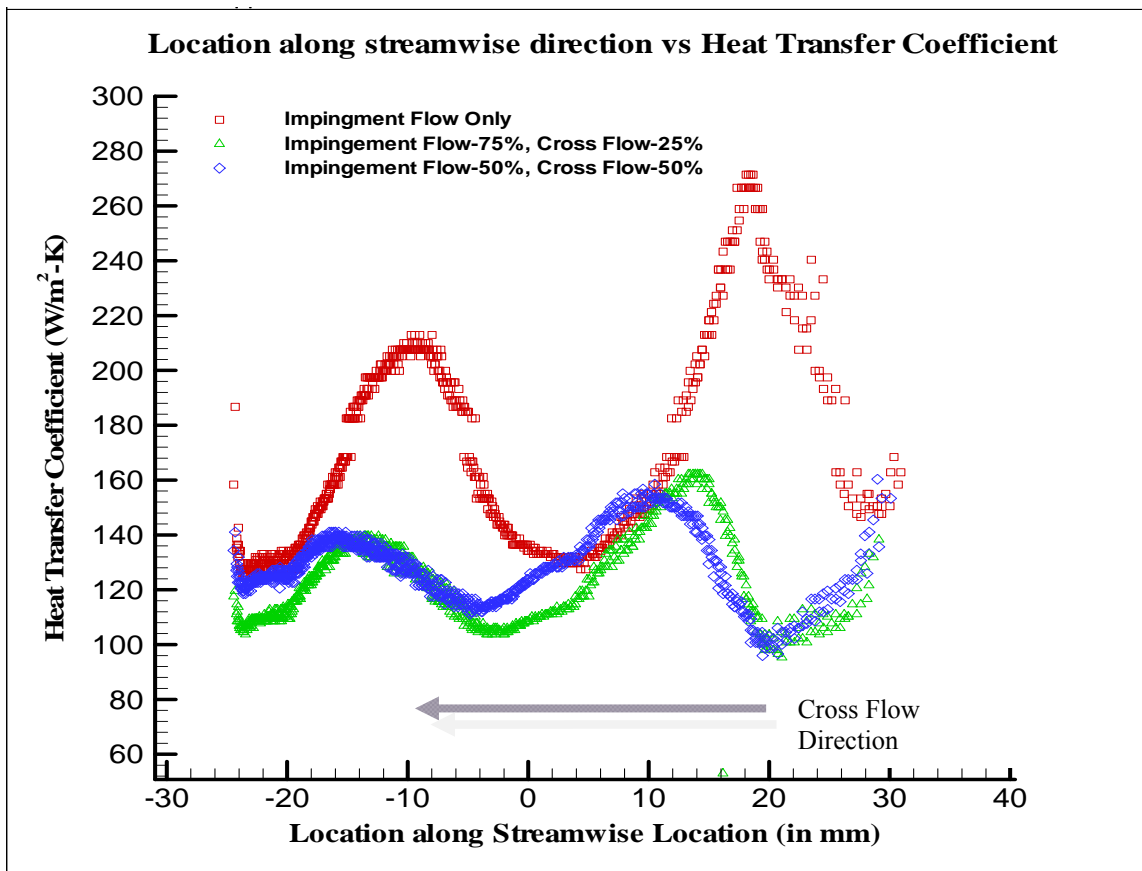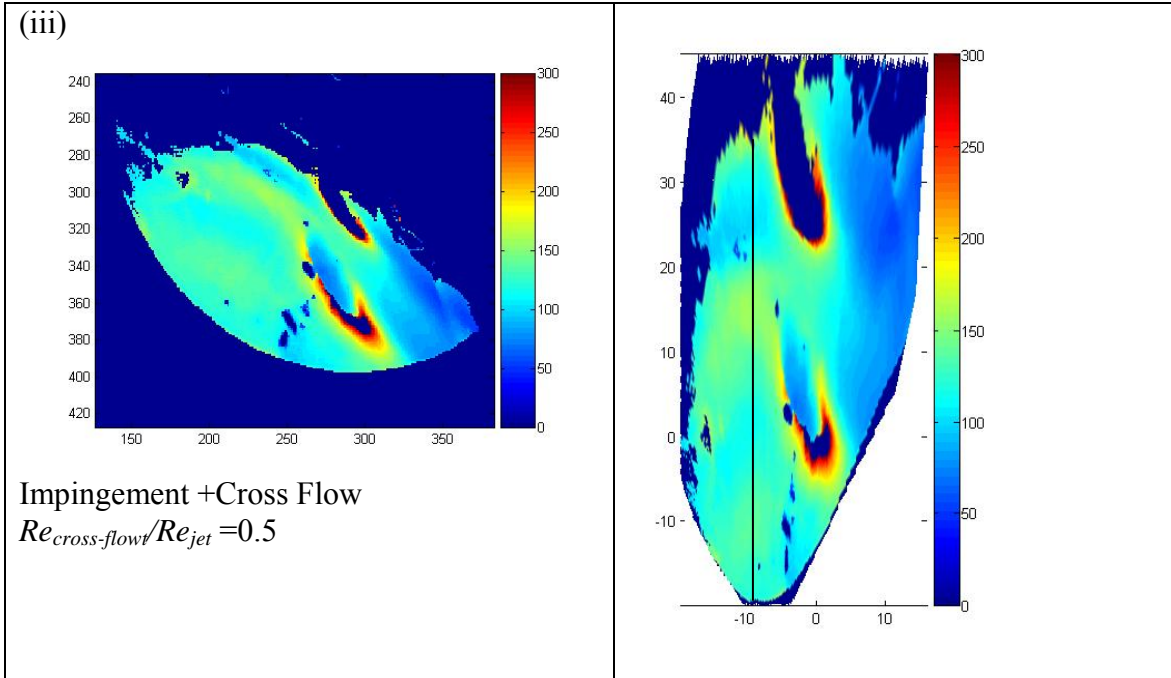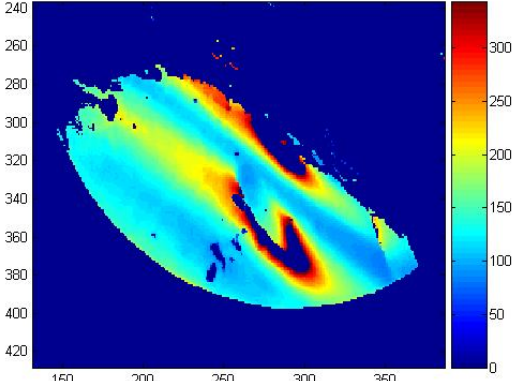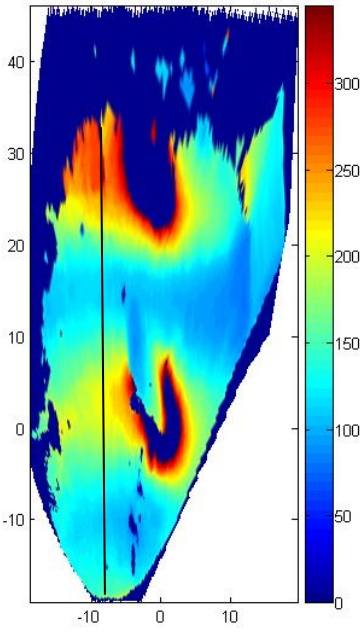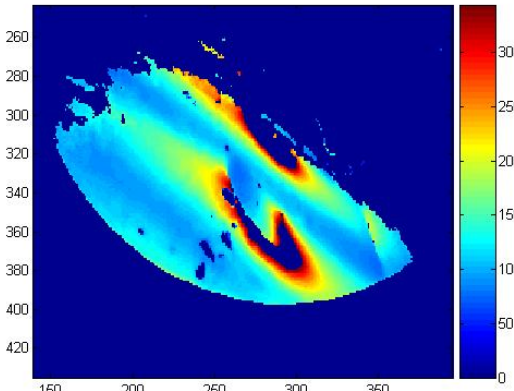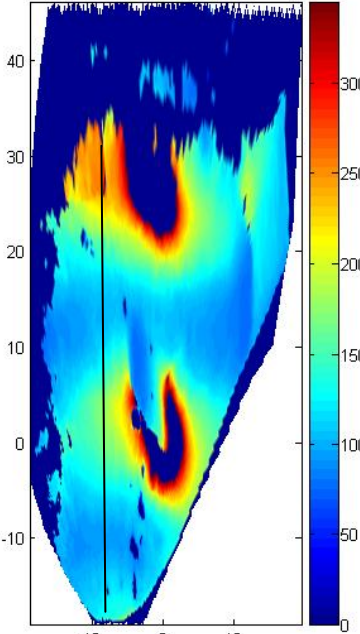

Fig 4.1: Line Plot for Case 1

Table 4.3 - Case 2: Rows 1-5 are Open, Tip is Closed

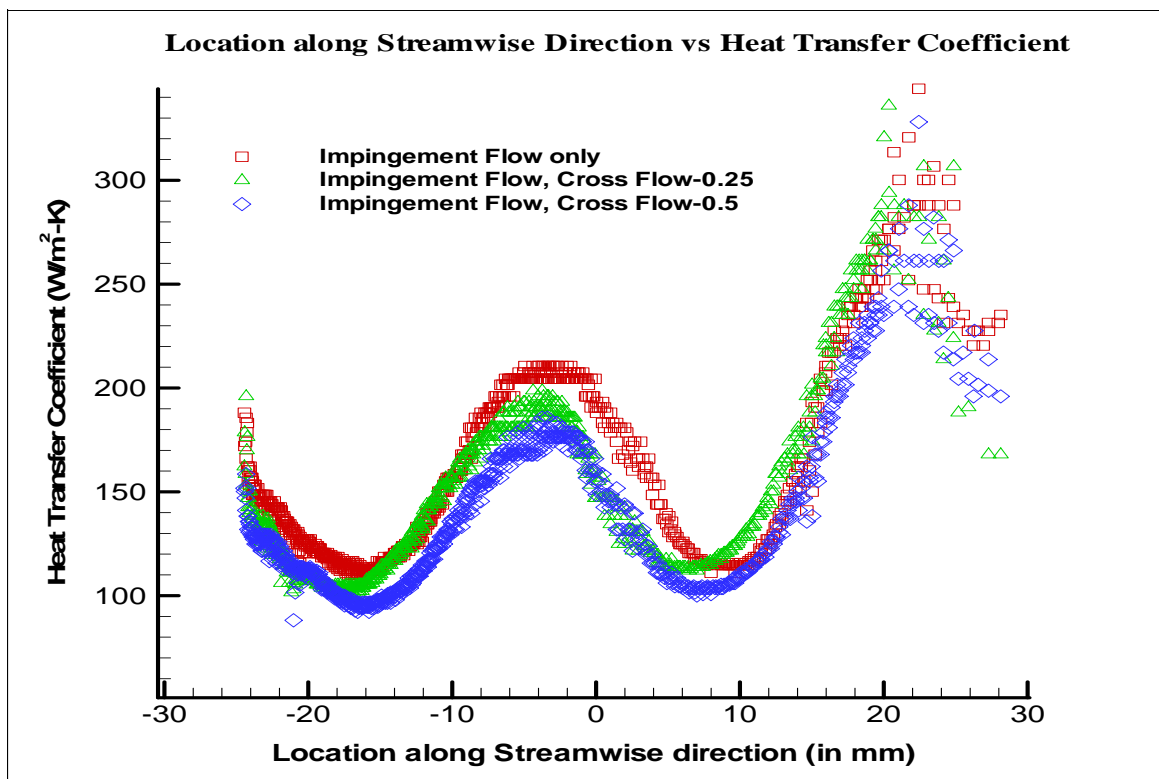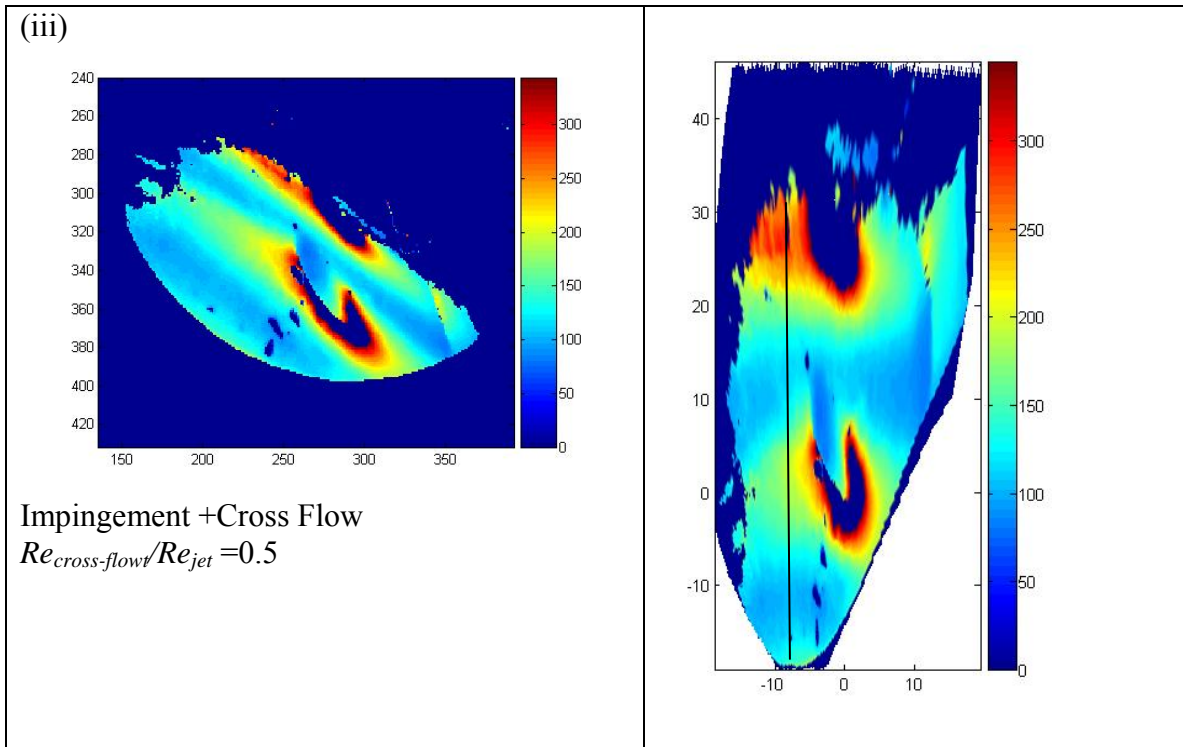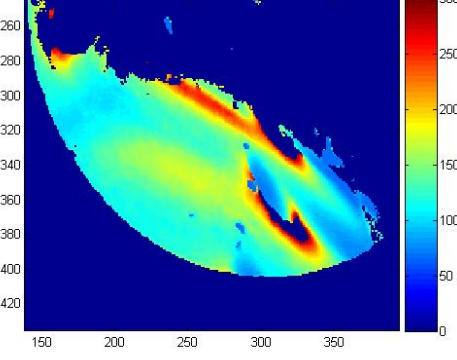| Liquid Crystal Image	Processed Heat Transfer Contour (h W/m^2-K)
(i) Pure Impingement Flow, $Re_{cross-flow}/Re_{jet}$ =26601	
(ii) Impingement +Cross Flow $Re_{cross-flow}/Re_{jet}$ =0.25	

(Table contd.)

(iii)

Impingement +Cross Flow
$Re_{cross-flow}/Re_{jet}$ =0.5
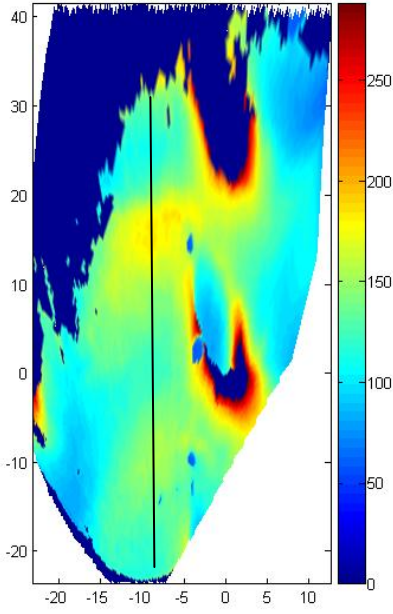
Fig 4.2: Line Plot for Case 2

Table 4.4 - Case 3: Rows 1-4 are Open, Row 5 (Gill Row) is Closed, Tip is Open

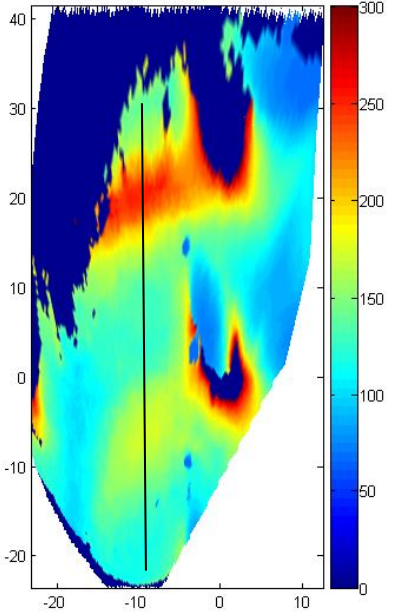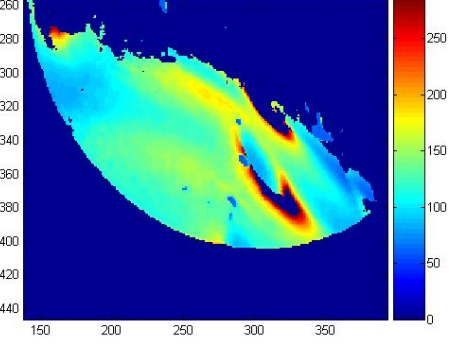| Heat transfer contour, camera view	Processed Heat Transfer Contour (h W/m^2-K)
(i) Pure Impingement Flow, Re_{jet} = 26432	
(ii) Impingement +Cross Flow $Re_{cross-flow}/Re_{jet}$ =0.25	

(Table contd.)

(iii)

Impingement +Cross Flow
$Re_{cross\text{-}flow}/Re_{jet}$ =0.5

Location along Streamwise direction vs Heat Transfer Coefficient
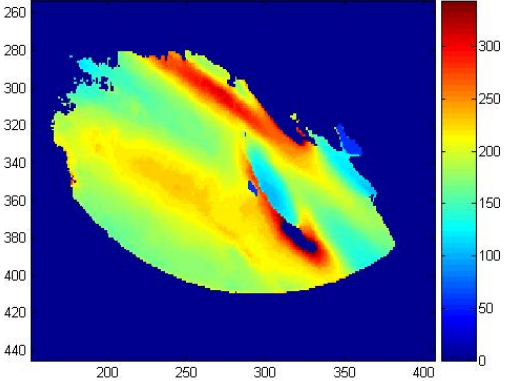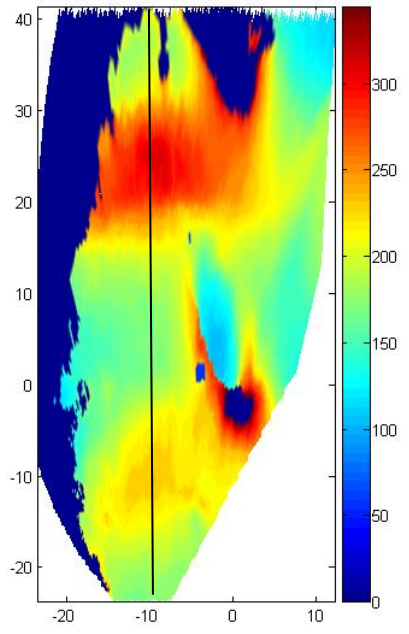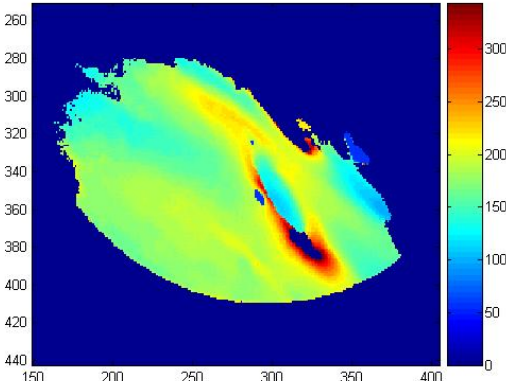
Fig 4.3: Line Plot for Case 3

Table 4.5 Case 4– Rows 1-3, Row 5 (Gill Row) are Open, Row 4 is closed, Tip Open

Heat transfer contour, camera view	Processed Heat Transfer Contour (h W/m^2-K)
(i) Pure Impingement Flow, Re_{jet} = 26107	
(ii) Impingement +Cross Flow $Re_{cross-flow}/Re_{jet}$ =0.25	

(Table contd.)

(iii)

Impingement +Cross Flow
$Re_{cross-flowt}/Re_{jet}$ =0.5

Location along Streamwise direction vs Heat Transfer Coefficient

□ Impingement Flow only
△ Impingement Flow, Cross Flow-0.25
◇ Impingement Flow, Cross Flow-0.5
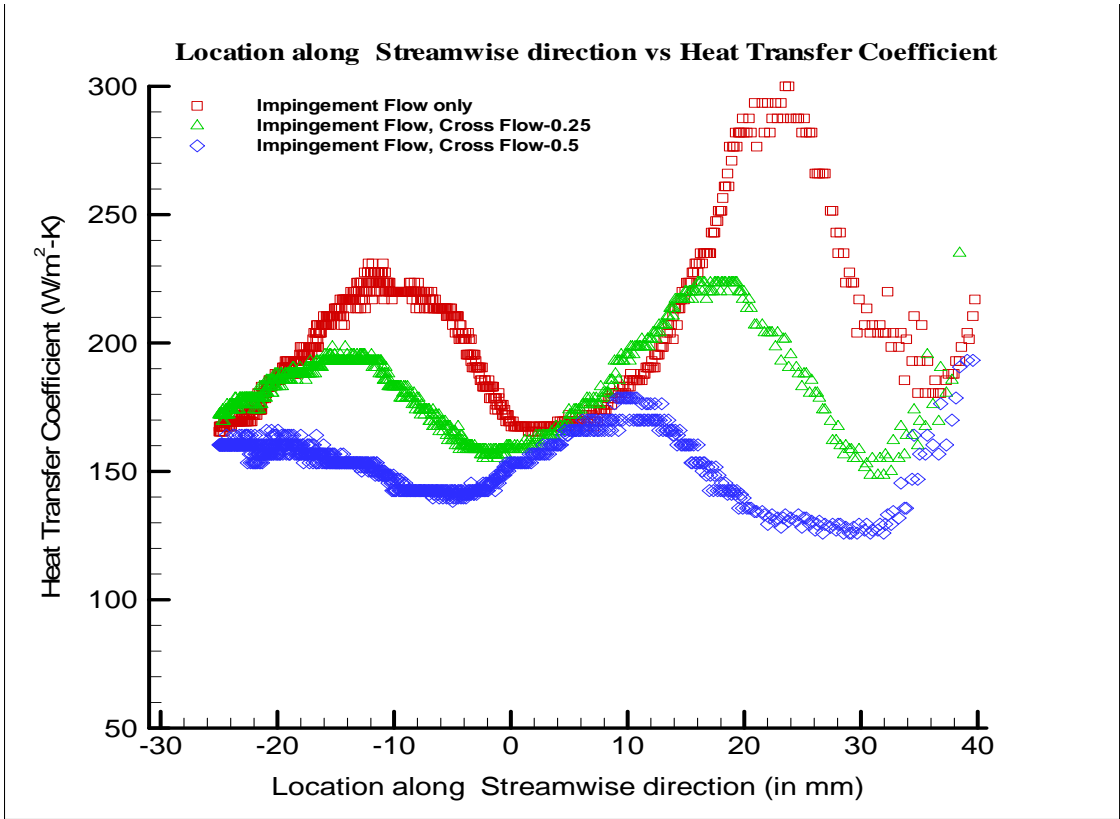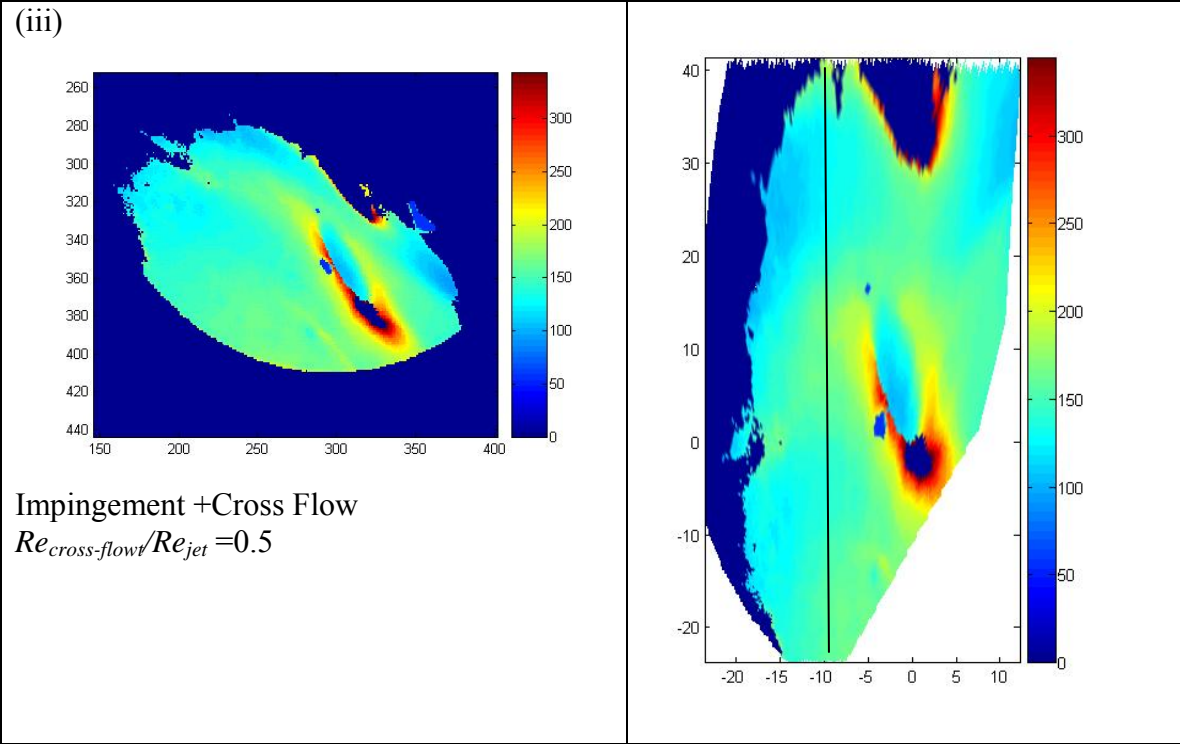
Fig 4.4: Line Plot for Case 4

Also there is a greater migration of the peaks in the downstream direction. The second impingement zone observed in Case 1 and Case 2 is only partially captured in the field of view in Case 5. All the film cooling holes are closed in Case 6 and the entire cross flow exits from the tip opening of the peanut cavity. As observed in all the previous cases the first instance with only pure impingement flow exhibits distinct impingement zones and the characteristic reduction in the heat transfer value away from the impingement zones. The cross flow is the predominant component in the instances with external cross flow completely smothering the impingement jet. The line plot in Fig 4.7 corroborates the observations in the contours. The peak heat transfer coefficient witnesses a 14 % decrease from Case 1(i) to Case 6(i).

4.1.2 Area Average of Heat Transfer Coefficients

Selection of an area to calculate the average value of heat transfer coefficient for all the cases is quite difficult since the impingement region location is different for each case depending on the flow configuration. The area selected to calculate the average value of the heat transfer coefficient encompasses half the pitch distance between consecutive film cooling holes and is shown in fig 4.7. The region of the film cooling hole is excluded from the chosen area. The average was calculated by adding up the heat transfer coefficient values at all the pixels within the selected area and then dividing this sum by the total number of pixels. For the area considered, in each Case, the average heat transfer coefficient is the highest for the case with pure impingement. This shows that though the uniformity of heat transfer has increased with increasing cross flow the associated decrease of heat transfer in the impingement zone drags down the average value of heat transfer coefficient.

Table 4.6 - Case 5: Rows 1-4 are Closed, Row 5 (Gill Row is Open), Tip is Open

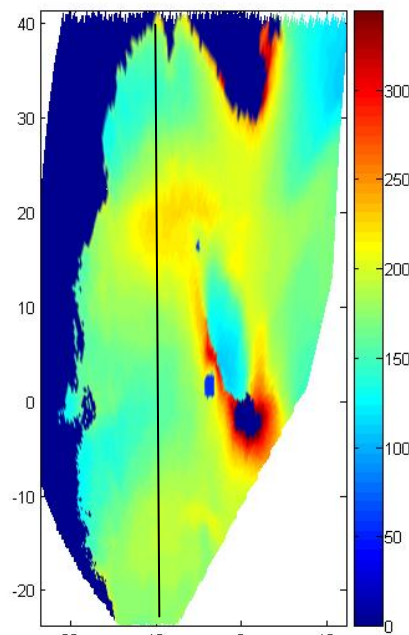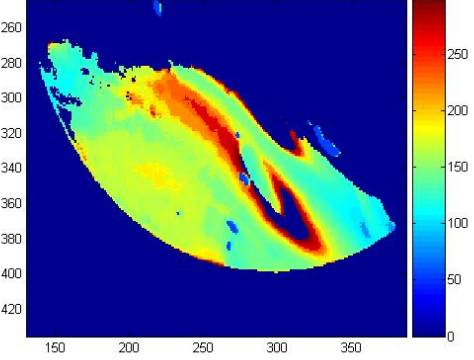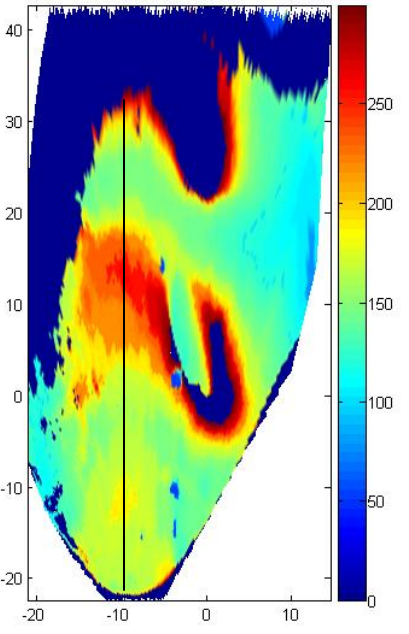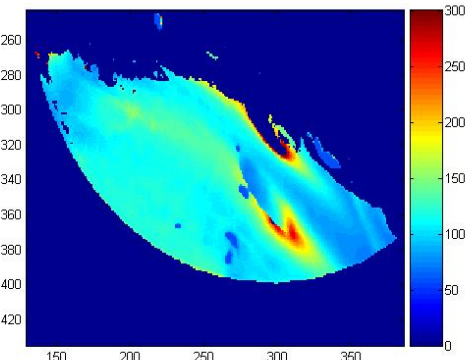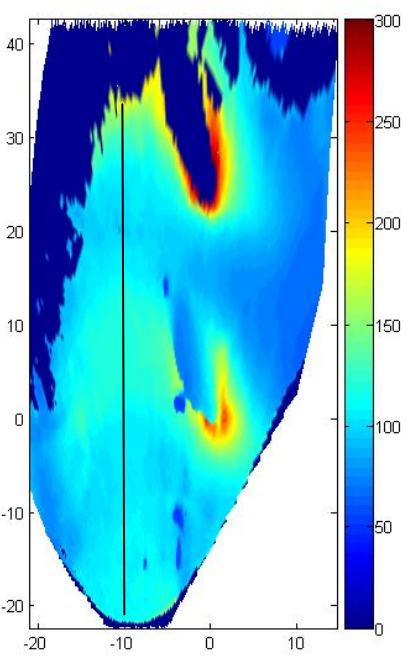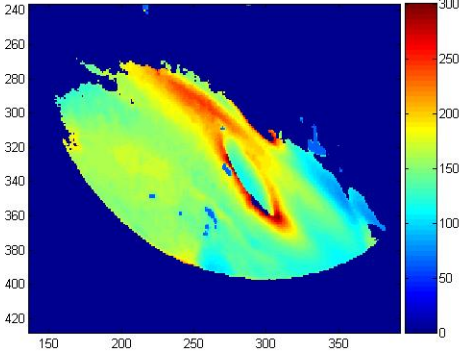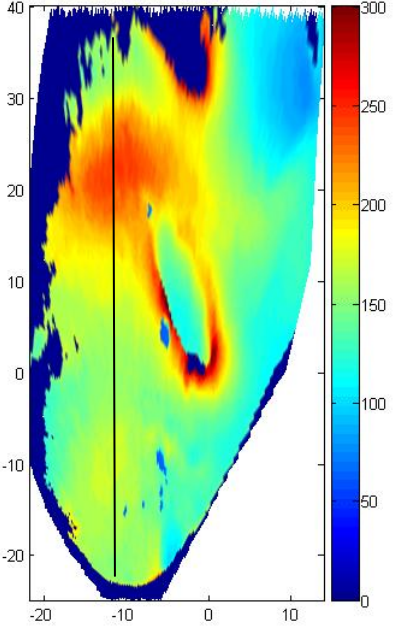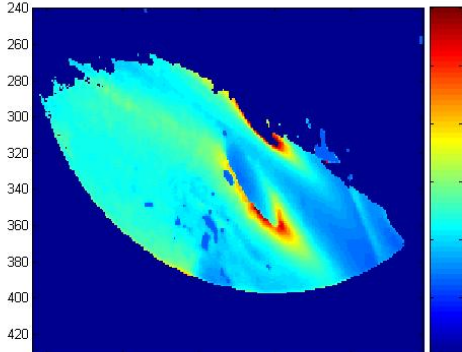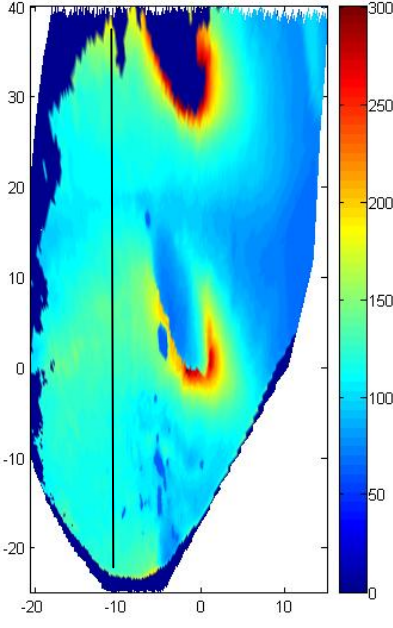| Heat transfer contour, camera view	Processed Heat Transfer Contour (h W/m^2-K)
(i) Pure Impingement Flow, Re_{jet} = 26432	
(ii) Impingement +Cross Flow $Re_{cross-flow}/Re_{jet}$ =0.25	

(Table contd.)

(iii)

Impingement +Cross Flow
$Re_{cross-flow}/Re_{jet} = 0.5$

Location along Streamwise direction vs Heat Transfer Coefficient

□ Impingement Flow only
△ Impingement Flow Cross Flow-0.25
◇ Impingement Flow, Cross Flow-0.5

Location along Streamwise direction (in mm)

Fig 4.5: Line Plot for Case 5

Table 4.7 - Case 6: Rows 1-5 are Closed, Tip is Open

Heat transfer contour, camera view	Processed Heat Transfer Contour (h W/m^2-K)
(i) Pure Impingement Flow, Re_{jet} = 26468	
(ii) Impingement +Cross Flow $Re_{cross-flow}/Re_{jet}$ =0.25	

(Table contd.)

54

(iii)

Impingement +Cross Flow

$Re_{cross\text{-}flow}/Re_{jet}$ =0.5
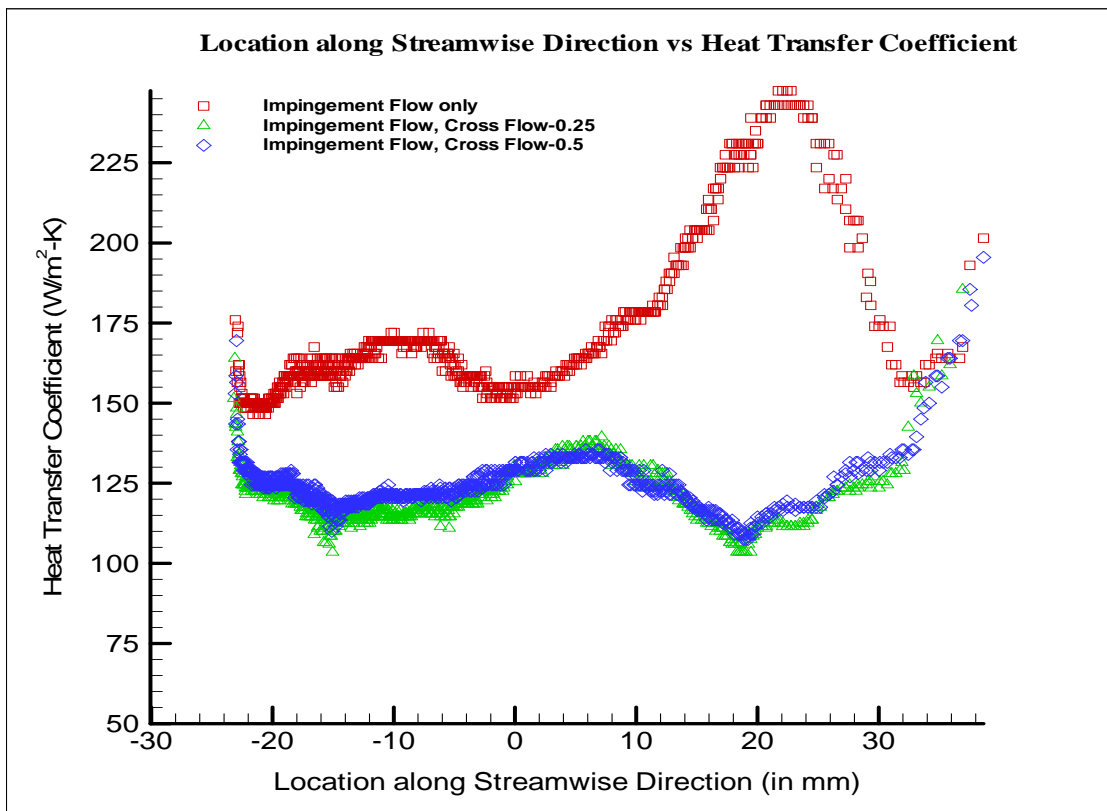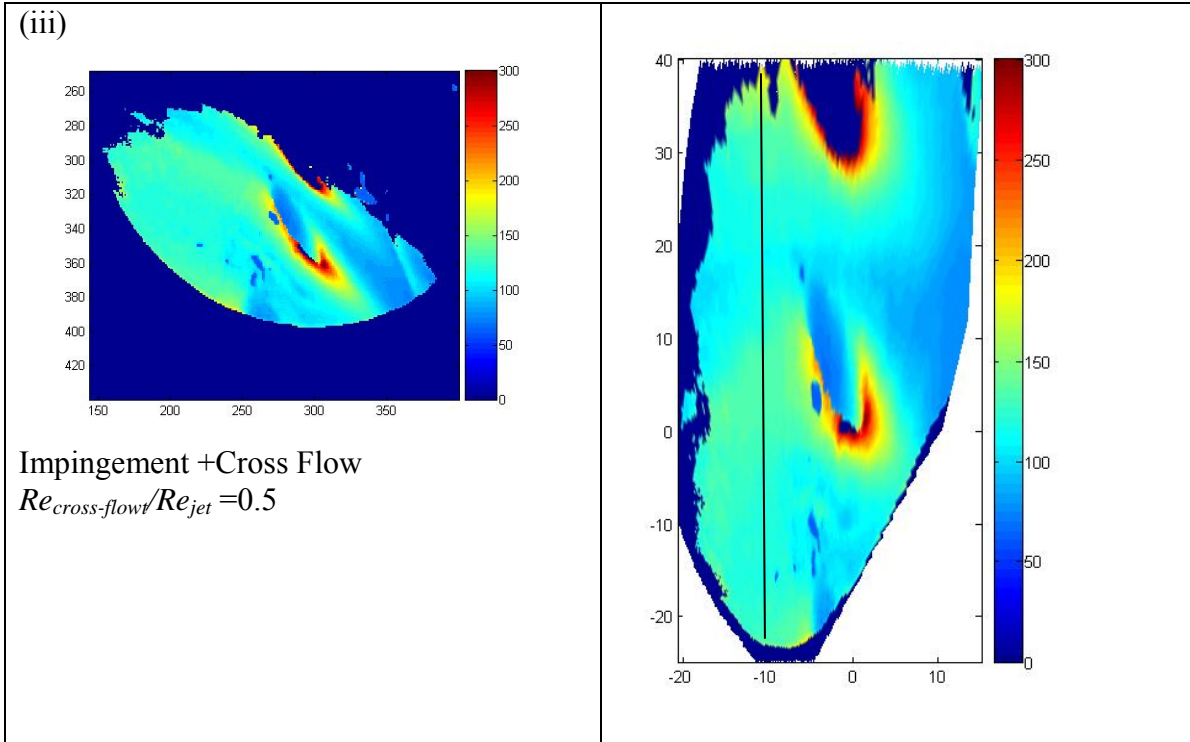
Fig 4.6: Line Plot for Case 6
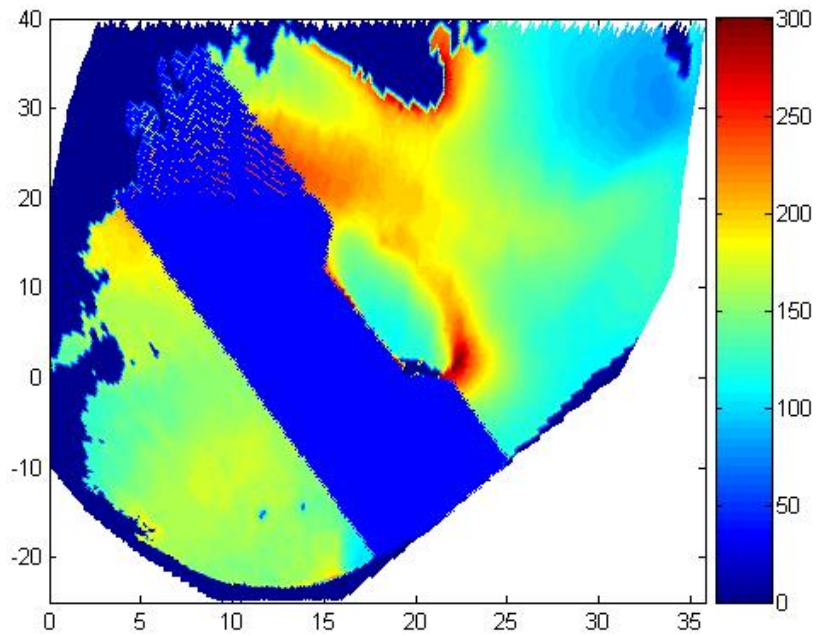
Fig 4.7: Area selected for average (Blue region)

Table 4.8 - Average value of heat transfer coefficients within the area shown in Fig 4.8

CASE	Area average of heat transfer coefficients (W/m^{2}K)
Case 1(i)	143
Case 1(ii)	128
Case 1(iii)	132
Case 2(i)	162
Case 2(ii)	150
Case 2(iii)	145
Case 3(i)	176
Case 3(ii)	108
Case 3(iii)	117
Case 4(i)	164
Case 4(ii)	119
Case 4(iii)	123
Case 5(i)	213
Case 5(ii)	186

(Table contd.)

Case 5(iii)	158
Case 6(i)	113
Case 6(ii)	111
Case 6(iii)	105

The average values of heat transfer are the lowest Case 6 owing to the relative lack of cross flow when compared to Cases 1-5. The average value of heat transfer seems to depend on not just the cross flow component but also the film cooling hole configuration. The exact extent to which each of these components affects the average value of heat transfer within the selected area cannot be ascertained.

4.2 Discussion of the Results

The magnitude of the maximum heat transfer coefficient and the location of the stagnation point of the jet depend on the following factors,

- Jet Dimensions

    o Height of the Jet

    o Diameter of the jet

- Pressure ratio across the impingement hole,

- Number of impingement holes

- Arrangement of impingement holes

- Angle of Impingement of the jet

- Presence of Cross Flow

- Number of rows of Film cooling holes open

- Combination in which the rows of film cooling holes are employed.

Among the above mentioned factors the first four i.e. Jet Dimensions, Pressure ratio, Number of Impingement Holes and Arrangement of Impingement holes are the same in

all the cases and hence can be considered to be constant. The Angle of Impingement is also constant but its effects on the displacement of the point of maximum heat transfer (Stagnation Point or Point of Maximum Mass Transfer) are discussed in detail in relevance to the results obtained. The major distinguishing factors are the final three factors which are the presence of cross flow, number of film cooling holes open and the combination in which they are employed. The roles of these factors in the obtained results are discussed in the subsequent sections.

4.2.1. Jet impingement on an inclined surface

The impingement of a jet on an inclined surface leads to the displacement of the stagnation point and the point of maximum heat transfer (PMHT) from the geometric impingement point (GIP) and a reduction in the magnitude of peak heat transfer coefficient. Also the final heat transfer contour is not symmetric about the axis of symmetry. This phenomenon has been observed in a number of studies on the impingement of a jet on oblique surfaces. Sparrow and Lovell, 1980, conducted experimental studies on the heat transfer characteristics of an obliquely impinging circular jet. The experiments encompassed a range of incidence angles from normal impingement to 30^0 and Reynolds number ranging from 2500 to 30000. It was observed that any deviation from the normal impingement caused a migration of the point of maximum heat transfer away from the GIP and a reduced peak heat transfer coefficient. Also, the displacement of PMHT and reduction in the magnitude of peak heat transfer coefficient increase with increasing inclination. It was also observed that neither the maximum pressure point nor the stagnation point may coincide with the PMHT as well as with each other. Crafton et al., 2006, conducted PIV measurements to locate the

stagnation point and the point of maximum pressure for jet angles 15^0, 30^0 and 45^0 angles at various impingement distances (i.e. height of the jet). The stagnation point and the point of maximum pressure were found to be located upstream (in the span wise direction) of the GIP along the axis of symmetry of the jet. These locations of the point of maximum heat transfer, stagnation point and point of maximum pressure were reported to be a strong function of the inclination angle and a weaker function of the impingement distance. Fig 4.8 below shows a comparison of the migration of stagnation point with respect to inclination angle as recorded by various studies. The various parameters shown in the Fig 4.8 are s_V = Displacement of stagnation point from GIP, H= Height of the jet, α= Inclination Angle, D= diameter of the jet. All the above studies also indicate a decrease in the magnitude of maximum heat transfer coefficient. The above results have been arrived at analytically by Dorrepaal, 1986 and numerically by Garg and Jayaraj, 1988. Figure 4.9 shows the increasing displacement of PMHT and reduction in the magnitude of peak heat transfer with increasing jet inclination. In the present study the inclination angle is constant for all the cases and has a value of θ =59.5^0 (i.e. α= 90-θ=30.5^0). A representative cross section is shown in Fig 4.10. The location of the point of maximum heat transfer seen in the heat transfer contours is a combination of the inclination angle and the effect of cross flow. It is however difficult to quantify the individual contribution of these components on the final location of the point of maximum heat transfer. All the cases (1-6) exhibit this phenomenon to varying degrees.

The movement of the point of maximum heat transfer as a result of the combination of inclination cross flow and inclination effect is in the range of 0.5D to O.7D. A more exact figure is difficult to arrive at since pinpointing the location of the
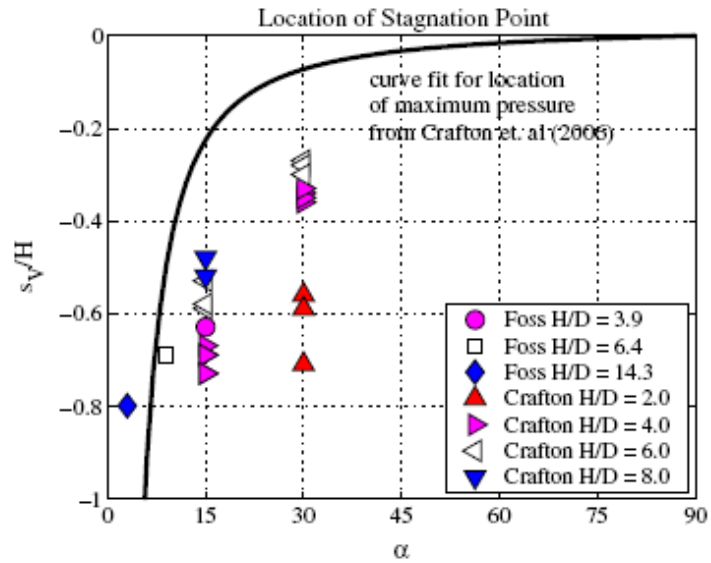
Fig 4.8: Deviation of the stagnation point from the geometric impingement point divided
by the impingement distance versus α (inclination angle)
Crafton et al, 2006
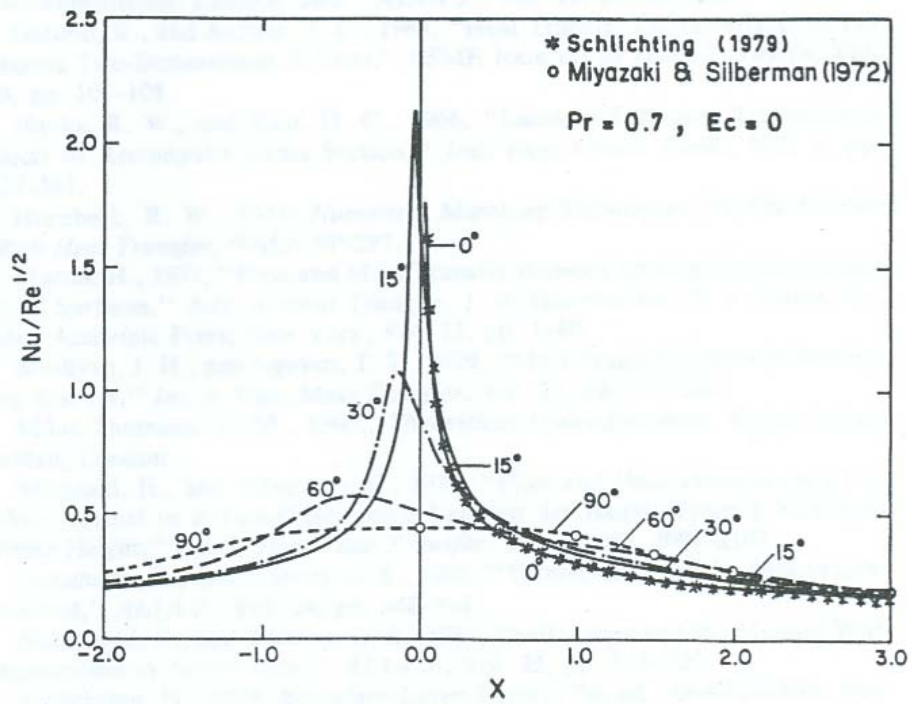
Fig 4.9: Migration of PMHT and the reduction in magnitude of peak heat tranfer
coefficient with increasing jet inclination
Ekkad and Han, 1997

stagnation point or the point of maximum heat transfer accurately is not possible using the current data. Figure 4.11 below shows the movement of the region of impingement from the GIP for case 5(i). The pitch line for all the holes through which the GIP passes is shown as a pink line at positive coordinate of 10 mm on the X-axis. The asymmetry of the heat transfer profile about the axis of symmetry (passing through the GIP) is evident from Fig 4.11.
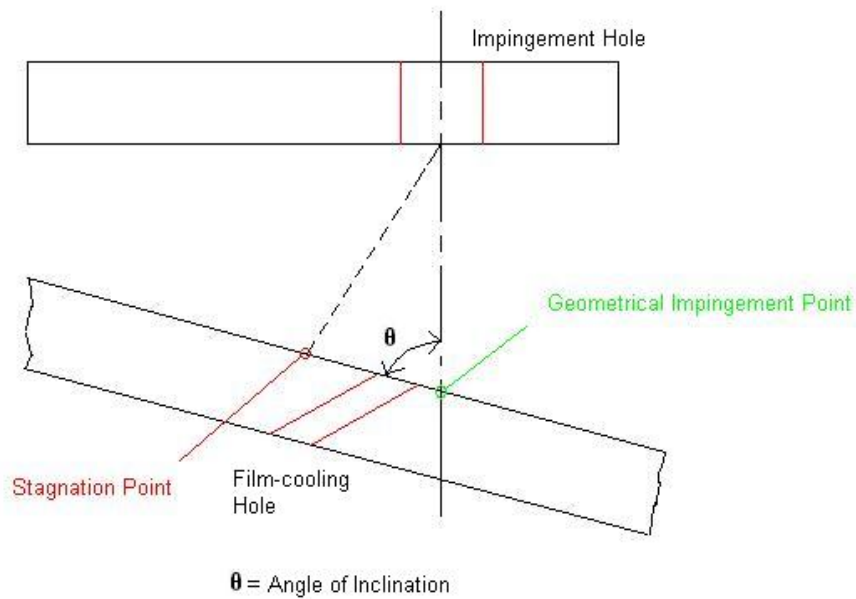
Fig 4.10: Displacement of stagnation point

4.2.2. Cross Flow Momentum Versus Jet Momentum

The cross flow component in each of the test cases consists of two components

- Spent flow from the upstream jets

- Independent cross flow introduced in the second and third instances of each case

The cross flow can affect the cooling performance in the following ways:

61

- It provides a buffeting effect to reduce cooling performance by reducing the impact of the jet flow on the surface.
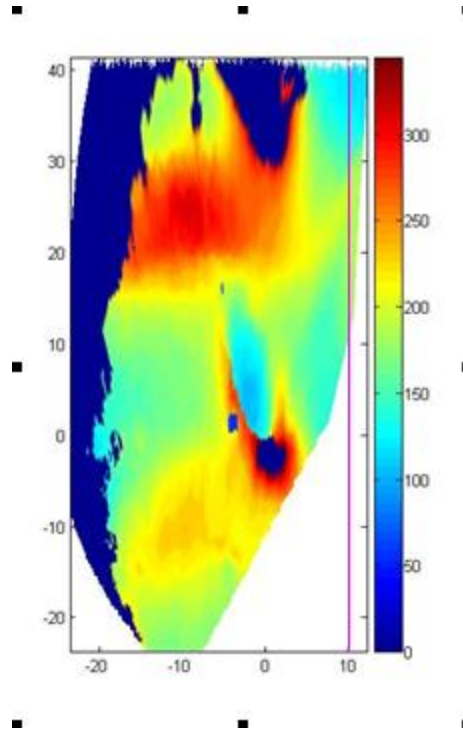
Fig 4.11: Movement of the Region of Impingement from the GIP for case 5(i).

- It displaces the jet in the direction of the stream and leads to more lateral spread in the span wise direction. The resulting jet structure is unique and is described in detail below.

- It can also provide some heat transfer enhancement through increased convective cooling due to increased mass flow rate the regions further away from the impingement point of the jet.

The jet as it moves away from the impingement hole acquires the shape of a horseshoe. This is a result of the interaction of the jet with the external flow. The intermixing of the emerging jet from the impingement hole with the deflecting cross flow

leads to the development of a turbulent layer. As explained in the Chapter one the peripheral particles of the jet have less velocity than the particles at the core of the jet. These peripheral particles which are in direct interaction with the cross flow are more forcefully bent and are moved along more curved trajectories which leads to the deformation of the circular jet into a horse-shoe structure. Figure 4.12 below illustrates the development of a counter rotating pair of vortices a.k.a. kidney pair of vortices within the jet under the influence of cross flow.

As the jet moves away from the impingement hole, the particles of the jet branch out more and more from the plane of symmetry and the legs of the horse shoe move apart. The deformation of the jet is observed to a greater or lesser extent in all the cases under study. The deformed structure of the jet is illustrated for the heat transfer contours of case 4(i) and case 5(i) in Fig 4.13. In the current cases under study, the jet momentum to external cross flow momentum is in the range of 6 to 8 because of which a clear development of kidney pair of vortices is not seen for the current height of the jet being employed. However, the deformation in the imprint clearly shows the effect of the cross flow. All the effects of cross flow described above compete with each other. There is a competing effect between the jet momentum and mass flow rate of the cross flow.

As the cross flow increases the ability of the jet to penetrate the cross flow is reduced. The above three effects act in tandem to give the final HTC contour, wherein, the heat transfer coefficient at the stagnation point is reduced but a more uniform HTC contour is obtained. This can be observed from the decrease in the slope of the curve in the line plots from pure impingement case to cases with increased cross flow.
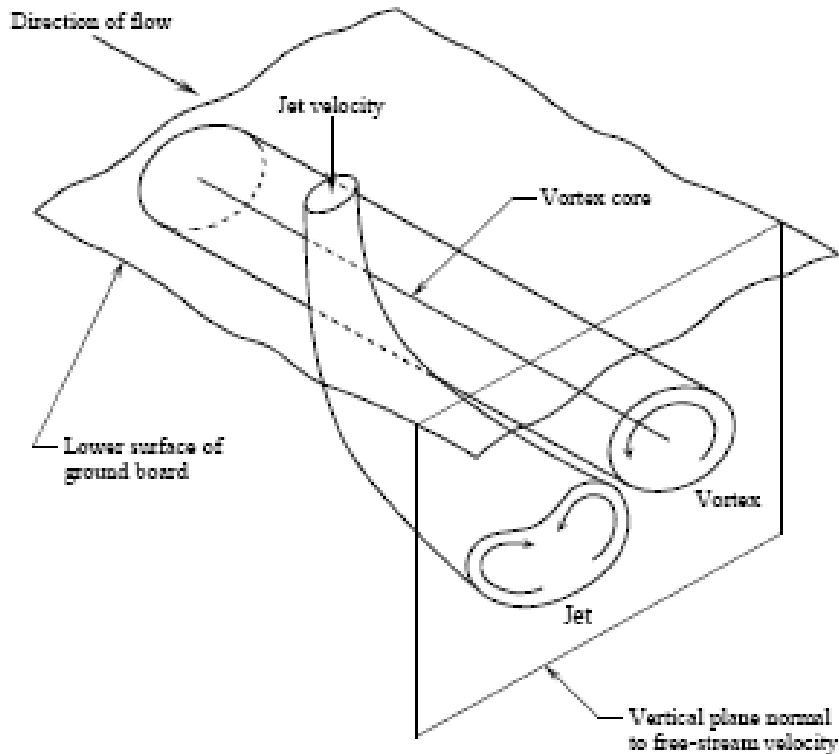
Fig 4.12: Development of a Horseshoe jet with counter rotating pair of vortices under the influence of cross flow, Lincoln, 2001

Also the local circulatory motion (the opposing vortices) within the horse shoe may contribute to a slight increase in the heat transfer. Such an effect was reported by Nakabe et al 1998. The exact extent to which each of the above factors affect the magnitude of heat transfer and the position of PMHT is difficult to predict without further information on the flow structure within the peanut cavity.

4.2.3. Film Cooling Holes Configuration

There are a total of five rows of film cooling holes on the target surface. Depending on the number of rows opened and the combination in which these rows are opened, the stagnation point is shifted accordingly. The combination and number of rows of film cooling holes used affects the stagnation point and the heat transfer distribution in the following ways:

- The total cross flow within the peanut cavity depends on the number of film cooling rows kept open. As the number of film cooling holes is reduced there is an increase in the cross flow. This leads to a greater deflection of the jet and consequently a greater loss of jet momentum. This leads to a reduction in the peak heat transfer coefficient. A minor increase in heat transfer away from the impingement region is observed due to increase in the convective cooling component.

Fig 4.13: Deformation of the circular jet under the effect of the cross flow for
Case 4(i) and Case 5(i)

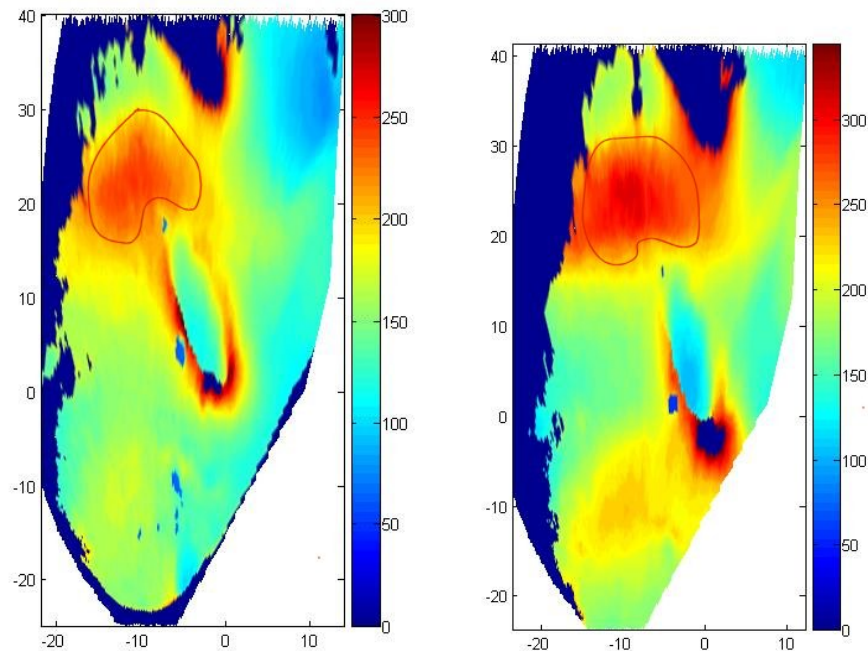- The film cooling holes provide a path of lesser resistance to the cross flow when it is interacting with the jet. Hence the combination in which the rows are used plays a part in determining the heat transfer distribution. This is the reason why a higher heat transfer is observed in case 5 when compared to case 2 though in both

the cases the same number of rows are kept open. In case 5 since the fourth showerhead row (the Film Cooling Hole shown in the images belongs to this row) is closed the cross flow is diverted away from the jet and hence we observe a higher heat transfer coefficient.

- The location of PMHT of the jet is contingent on the direction in which the cross flow is diverted. As the flow is diverted through the film cooling holes the PMHT is deflected toward the hole. This effect is observed strongly in Case 2 where the entire flow exiting the peanut cavity is routed through the film cooling holes.

4.2.4 Flow Path of Least Resistance

The Jet and the Cross Flow follow a path of least resistance. The Jet and the cross flow act as inhibitors to each other. Also the flow path of the jet in the peanut cavity is decided by the configuration of the film cooling holes and the tip condition. For the tip open cases, a path of lesser resistance towards the tip exists which promotes more cross flow and hence the impingement point of the jet is moved further downstream. In case 2, however, the tip is closed and hence the Jet tends to move towards the corresponding film cooling holes and hence an effective point of impingement is lost. Therefore we see a decrease in the maximum heat transfer coefficient. Similarly the configuration of film cooling holes also affects the location of the impingement point of the jet. There is no direct impact on the location of the impingement point but the changes in configuration changes the flow path for the spent flow and external cross flow.

Chapter 5

Conclusions

A novel Camera-Endoscope based Liquid Crystal technique was used to study the heat transfer behavior of a Jet Impingement cooling system under different film cooling configurations and cross flow conditions. The study was conducted on scaled model of the leading edge cavity of turbine vane. Heat transfer distribution on the target surface was obtained for all the cases listed in Table 4.1. A comparison of the heat transfer distributions indicates that external cross flow has a negative effect on the peak value of heat transfer but creates a more uniform distribution. This trend is observed in all the cases. The film cooling configuration plays a significant role in the determination of the location of the impingement zone and the distribution of heat transfer. Case 5 exhibits a higher heat transfer and a more uniform distribution than Case 1 though both have the same number of film cooling rows open. The peak heat transfer value in each of the cases seems to depend more on the extent of cross flow than on the film cooling configuration. Closing the tip seems to be unsuitable for this geometry since the effective impingement of the jet is lost as illustrated in Case 2 although there is an increase in the peak heat transfer. However, this condition might be remedied by displacing the impingement zone away from the film cooling hole. This may be achieved by either shifting the impingement holes with respect to the film cooling holes or by altering the geometry of the target surface.

A further study of the flow structure within the peanut cavity is required to determine the exact effect of the test parameters on the Impingement location and to determine the quantify the suggested alterations in the geometry.

References

1. www.lag.ensieg.inpg.fr/bouziani/Research2.htm

2. http://www.me.umn.edu

3. Gas Turbine Heat Transfer and Cooling technology, Han J.C., Dutta S, Ekkad S.V., Taylor and Francis, 2000

4. Bruchez, J. P. and Goldstein, R. J., 1975, "Impingement Cooling from a Circular Jet in a Crossflow," Int. J. of Heat Mass Transfer, Vol. 13, 1975, 719-730.

5. Chance J. L., 1974, "Experimental Investigation of Air Impingement Heat Transfer under an Array of Round Jets," TAPPI vol. 57, no. 6, pp. 108-112

6. Crafton J, Campbell C, Elliott G, Sullivan J, 2006, 'The impingement of sonic and sub-sonic jets onto a flat plate at inclined angles', Experiments in Fluids, Springer-Verlag, No. 41, pg 699-710

7. Downs, S. J., and James, E. H., 1987, "Gas Impingement Heat Transfer - a Literature Survey," ASME Paper No. 87-HT-35.

8. Dorrepaal J.M., 1986,'An exact solution of the Navier–Stokes equation which describes non-orthogonal stagnation-point flow in two dimensions', J Fluid Mech 163, pg 141–147

9. Ekkad, S. V., and Han, J. C., 1997, " Detailed Heat Transfer Distributions in Two-Pass Square Channels with Rib Turbulators," Int. J. Heat and Mass Transfer, Vol.40, No. 11, pp.2525-2537.

10. Florschuetz, L. W., 1982, "Jet Array Impingement Flow Distribution and Heat Transfer Characteristics," NASA CR 3630.

11. Florschuetz, L. W., Berry, R. A., and Metzger, D.E., 1980, "Periodic Streamwise Variation of Heat Transfer Coefficients for Inline and Staggered Arrays of Circular Jets with Crossflow of Spent Air," J. of Heat Transfer, Vol. 102, No.I, pp. 132-137.

12. Florschuetz, L. W., Truman, C. R., and Metzger, D.E., 1981, "Streamwise Flow and Heat Transfer Distribution for Jet Impingement with Crossflow," J. of Heat Transfer, Vol. 103, No.2, pp. 337-342.

13. Florschuetz, L. W., Metzger, D.E., Su, C.C., Isoda, Y., Tseng, H. H., 1984, "Heat Transfer Characteristics for Jet Array Impingement with Initial Crossflow," J. of Heat Transfer, Vol. 106, No.l, pp. 34-41

14. Florshuetz, L.W., Metzger, D.E., and Truman, C.R., 1981, "Jet Array Impingement with Crossflow Correlation of Streamwise Resolved Flow and heat Transfer Distributions," NACA CR-3373,.

15. Foss J.F., Kleis S.J., 1972,'The oblique impingement of an axisymmetric jet', NASA Technical Report 23-004-068

16. Galant S. and Martinez G., 1982, "Crossflow Influence upon Impingement Convective Heat Transfer in Circular Arrays of Jets, A General Correlation," Proceedings of the 7 th International Heat Transfer Conference, pp. 343 -348.

17. Garg, V. K., Jayaraj S, 1988, 'Boundary layer analysis for two-dimensional slot jet impingement on inclined plates', Trans. of the ASME, Vol 110, pg 577-582

18. Gau, C and Chung, C.M., 1991, "Surface curvature Effect on Slot-Air-jet Impingement Cooling Flow and Heat Transfer Process," Trans. of the ASME, Vol. 113, pp. 858–864.

19. Goldstein, R. J. and Timmers, J. F., 1982, "Visualization of Heat Transfer from Arrays of Impinging Jets," Int. J. Heat and Mass Transfer Vol. 25, Dec. 1982, pp 1857-1868

20. Holdeman J. D., 1983, "Perspectives on the Mixing of a Row of Jets With A Confined Crossflow," Lewis Research Center.

21. Huang, G. C., 1963, "Investigation of Heat Transfer Coefficients for Air Flow through Round Jets Impinging Normal to a Heat Transfer Surface," ASME Journal of Heat Transfer, Vol.85, 1963, pp. 237-243.

22. Huang, P. G., Mujumdar, A.S. and Douglas, W.J., 1984, "Numerical Prediction of Fluid Flow and Heat Transfer Under a Turbulent Impinging Slot Jet with Surface Motion and Crossflow," ASME paper 84-WA/HT-33.

23. Huang, Y., Ekkad, S. V., and Han, J.C., 1998, "Detailed Heat Transfer Distributions Under an Array of Orthogonal Impinging Jets," AIAA J. of Thermophysics and Heat Transfer, Vol. 12, No. 1, pp. 73-78.

24. Humber, A.M., and Viskanta, R., 1994, "Comparison of convective Heat Transfer to Perimeter and Center Jets in a Confined, impingement Array of Axis-symmetric Air Jets," International Journal of Heat and Mass Transfer, vol. 37, pp. 3025-3030.

25. Kercher, D. M. and Tabakoff, W., 1969, "Heat Transfer by a Square Array of Round Air Jets Impinging Perpendicular to a Flat Surface Including the Effect of Spent Air," ASME paper 69-GT-4, March, 1969.

26. Kline, S. J. and McClintock, J., 1953, "Describing Uncertainties in Single-Sample Experiments," Mechanical Engineering, Vol. 75, pp. 3-8

27. Lin, M., Wang, T. and Bunker, R.S., 2000, "Flow and Heat transfer of Confined Impingement Jets Cooling", ASME Turbo Expo, Paper #2000-GT-223

28. Lincoln P.E. , 2001, 'A Parametric Study of Jet/Vortex Interactions in the AMRL Water Tunnel', Aeronautical and Maritime Research Laboratory DSTO-TR-1209

29. Livingood, J.N.B., and Hrycak, P., 1973, "Impingement Heat Transfer from Turbulent Air Jets to Flat Plates - A Literature Survey," NASA TM X-2778.

30. Martin, H., 1977, "Heat and Mass Transfer between Impingement Gas Jets and Solid Surfaces," Advances in heat Transfer, Vol. 13, Academic Press, New York, pp. 1-60.

31. Metzger, D. E., Yamashita, T., and Jenkins, C. W., 1969, "Impingement Cooling of Concave Surfaces with Lines of Circular Air Jets," Journal of Engineering of Power, Vol. 91, pp. 149-152.

32. Nakabe K et al, 1998,'Generation of longitudinal vortices in internal flows with an inclined imping jet and enhancement of target plate heat transfer', International Journal of Heat and Fluid Flow, Vol 19, pg 573-581

33. Saunter, M., Clouser, S., and Han, J. C., "Determination of Surface Heat Transfer and Film Cooling Effectiveness in Unsteady Wake Flow Conditions." AGARD Conference Proceedings 527, pp. 6-1 to 6-12, 1992

34. Sparrow E.M., Lovell B.J., 1980, 'Heat Transfer Characteristics of Obliquely Impinging Circular Jet', Trans. of the ASME, Vol 102, pg 202-209

35. Taslim, M.E., Setayeshgar, L., 2001, 'Experimental Leading-Edge Impingement Cooling Through Racetrack Crossover Holes', ASME, Paper # 2001-GT-0153,

36. Taslim, M.E., Setayeshgar, L. and Spring, S.D. , 2001, 'An Experimental Evaluation of Advanced Leading Edge Impingement Cooling Concepts,' J. of Turbomachinery, Vol.123, No. 2, pg 147-153

37. Van Treuren, K. W., Wang, Z., Ireland, P. T., and Jones, T. V., 1994, "Detailed Measurements of Local Heat Transfer Coefficient and Adiabatic Wall Temperature Beneath an Array of Impingement Jets," Journal of Turbomachinery, Vol. 116, No. 2, 1994, pp. 369-374.

38. Viskanta, R., 1993, "Heat Transfer to Impinging Isothermal Gas and Flame Jets," Experimental Thermal and Fluid Science, Vol. 6, pp. 111-134.

Vita

Amar Jeetendra Panchangam Nivarthi was born in May 1982, to Mr. Rama Murthy Panchangam Nivarthi and Ms. Sulochana Panchangam Nivarthi in Anantapur, India. He attended St. Anthony's High School and finished his Intermediate in Mathematics and Science from St. Mary's Junior College. He then earned his Bachelor of Engineering degree in Mechanical Engineering from University College of Engineering, Osmania University, Hyderabad, India. Amar then pursued his Master of Science in Mechanical Engineering from Louisiana State University, Baton Rouge, under the guidance of Dr. Shengmin Guo and Dr. Sumanta Acharya. Having fulfilled the requirements set by the Graduate School and the Department of Mechanical Engineering Amar will graduate in May 2008.